

Drop Electro-Bouncing in Low-Gravity

by

Erin Stivers Schmidt

A thesis submitted in partial fulfillment of the
requirements for the degree of

Master of Science
in
Mechanical Engineering

Thesis Committee:
Mark Weislogel, Chair
Raúl Bayoán Cal
Gerald Recktenwald

Portland State University
2018

Abstract

We investigate the dynamics of spontaneous jumps of water droplets from electrically charged superhydrophobic dielectric substrates during a sudden step reduction in gravity level. In the brief free-fall environment of a drop tower, with a non-homogeneous external electric field arising due to dielectric surface charges (with surface potentials 0.4-1.8 kV), body forces acting on the jumped droplets are primarily supplied by polarization stress and Coulombic attraction instead of gravity. This electric body force leads to a droplet bouncing behavior similar to well-known phenomena in $1-g_0$, though occurring for much larger droplets (~ 0.5 mL). We show a simple model for the phenomenon, its scaling, and asymptotic estimates for droplet time of flight in two regimes: firstly, in short-times close to the substrate when drop inertia balances Coulombic force due to net free charge and image charges in the dielectric substrate, and secondly, in long-times far from the substrate when drop inertia balances free charge Coulombic force and drag. The droplet trajectories are controlled primarily by the dimensionless electrostatic Euler number \mathbb{E}_u , which is a ratio of inertial to electrostatic forces. To experimentally determine values of \mathbb{E}_u we conduct a series of drop tower experiments where we observe the effect of droplet volume, net free charge, and static surface potential of the superhydrophobic substrate on droplet trajectories. We use a direct search optimization to obtain a Maximum Likelihood Estimate for drop net charge, as we do not measure it directly in experiment. For $B\mathbb{E}_u/8\pi > 1$ droplets escape the electric field, however we do not observe any escapes in our dataset. Finally, with an eye towards engineering applications we consider the results in light of the so-called low-gravity phase separation problem with a short space system design worked example problem.

To Mom, Laura, and the DDT team

Acknowledgements

This work was supported by NASA Cooperative Agreement NNX12A047A. I am also greatly indebted to Andrew Greenberg for his frequent and sage technical advice, and to Joe Shields for his assistance with drop tower experiments.

Contents

Abstract	i
Acknowledgements	iii
1 Introduction	1
1.1 Spontaneous Drop Jump	3
1.2 Drop Electro-Bounce	4
1.3 Applications	8
1.4 Overview of this Thesis	9
2 Theory	10
2.1 Forces and the Equation of Motion	10
2.2 The Electric Field	14
2.3 Scaling	16
2.3.1 Inertial Electro-Image Limit	16
2.3.2 Inertial Electro-Viscous Limit	17
2.4 Asymptotic Estimates	18
2.4.1 Inertial Electro-Image Limit	18
2.4.2 Inertial Electro-Viscous Limit	19
2.5 Summary	20
3 Methodology	26
3.1 Overview	26
3.2 Experimental Methods	27
3.3 Data Reduction	34
3.4 Parameter Estimation	34
3.4.1 Inverse Problems	35
3.4.2 Smoothing	37
3.4.3 Optimization	38
3.4.4 Identifiability	43
3.5 Summary	47

4 Results	49
4.1 Parameter Estimates	49
4.2 Scale Quantities	50
4.3 Impact Dynamics	53
4.4 Conclusions	56
Appendices	
A Parallel Plate Method	58

List of Figures

3.3	The Furmidge model of the hysteresis of the contact line plotted as a function of static contact angle θ , and roll-off angle α , for 1 mL drops. The measured static contact angles, and roll-off angles of several superhydrophobic surfaces including the laser-etched PMMA used in this work are also shown annotated with the characteristic roughness lengthscale R_q of the surface.	31
3.4	SEM image of the superhydrophobic surface.	32
3.5	Charge decay in the dielectric laminates for several numbers of layers.	33
3.6	(a) Schematic noisy droplet trajectory data. We see that 1D Gaussian convolution and Wiener filters suffer from significant end effects. At this scale Butterworth and Savitsky-Golay filters are nearly indistinguishable. (b) Comparing Butterworth and Savitsky-Golay filtered first derivatives of the above schematic trajectory we see that the Butterworth filter also suffers from a slight end effect. This implies that the optimization will find a different optima of the likelihood depending on which type of filter is used.	39
3.7	The power spectra has a peak at 1 Hz, which is the drop trajectory parabola itself, and smaller peaks in the kHz range corresponding to various noise frequencies. The Savitsky-Golay and Butterworth filters seem to have the least distortion of the power spectra of the true signal. Both also attenuate the noise at the 2 kHz peak.	40
3.8	As is typical with Nelder-Mead much of the improvement in χ^2 is realized in the first few iterations. Overall the rate of convergence is sub-linear, which is to be expected for non-linear constrained problems using an heuristic algorithem.	43
3.9	A series of filtered drop trajectories arranged by increasing apoapse. The blue dots represent either the beginning and end of the experiment, or points at which the drop is either coming into, or leaving contact with the surface.	44
3.10	A series of drop trajectories showing the results of the parameter estimation. The trajectories are shown only up to the apoapse of the first bounce. The (—) lines show the ODE solution with given the MLE parameter vector. χ^2 goodness-of-fit varies between 1×10^{-5} and 1×10^{-8} with the better fit occurring typically for the drops with the lowest apoapses.	45

4.1	Covariance plot of main parameters E_0 , U_0 , droplet area ($V_d^{2/3}$), and q	50
4.2	Charge q , as a function of V_d , φ_s	51
4.3	Drop trajectories as a function of Eu.	52
4.4	Simulated forces acting on the drop. Experiments are shown by order of increasing apoapse.	53
4.5	Non-dimensional trajectories with the short-time scaling.	54
4.6	Dimensional time of flight asymptotic estimates t_f compared with experimental bounce times.	55
4.7	Experimental covariance between Eu and Im.	56

Chapter 1

Introduction

“When the influence of gravity on fluid behavior is diminished or removed, other forces, otherwise of small significance, can assume paramount roles.” - NRC Report to NASA, 2003[**motil’priorities’2012**]

Our terrestrially born intuition about how liquids flow is easily confounded in a low-gravity environment. This should come as little surprise, as we are creatures evolved at the bottom of a gravity well; gravity is natural to us. However when the magnitude of gravitational body forces become small, other forces come into play in fluid dynamical problems, which are otherwise negligible under normal circumstances in $1-g_0$. Our $1-g_0$ cognitive bias then leads to a plethora of problems which are both simultaneously trivially easy to solve in $1-g_0$, and which despite decades of study continue to elude solutions in a low-gravity context. One example of these problems is the so-called “phase separation” problem of separating a gas phase from a multi-phase flow (or the reverse case), without the aid of buoyancy due to gravity. Sans buoyancy, otherwise mundane activities such as venting a gas or settling a liquid in a tank become problematic[**petrash’controlling’1964**]. Trapped bubbles can vapor lock life-support, power, or propulsion systems[**jenson’passive’2014**]. Issues of phase separation have so bedeviled human endeavors in space that an entire Apollo Saturn 1B mission (AS-203) was earmarked to study them[**hastings’saturn’1965**]. This problem has for some time motivated a quest for substitute body forces, and the present work follows in that well-worn tradition.

A solid beginning to rectifying our problem of poor low-gravity intuition, would be to quantify how wrong our intuition is. First, let us clear up a common misnomer about the state of “zero-gravity”. The theory of general relativity is based on a fundamental equivalence of gravity and acceleration. By measuring acceleration alone, one cannot determine whether one is in

gravity-free space or free-falling in a gravitational field (or conversely whether or not one is uniformly accelerating, or standing at rest in a gravitational field). This is sometimes called the equivalence principle of general relativity (e.g. the equivalence of gravitational and inertial mass). In theoretical terms, a zero-g experiment performed in a drop tower on the surface of the Earth is equivalent to the same experiment performed in the nearly gravity-free deep space between galaxies, despite the fact that the drop tower itself is enveloped in a $1-g_0$ gravity field, where $g_0 = 9.81 \text{ m/s}^2$ is the standard gravitational acceleration at sea-level . At the orbital altitude of the International Space Station (ISS) the gravity level is still nearly 90% of its value at sea-level on Earth, but the astronauts aboard ISS feel weightlessness because they are in a state of free-fall. In a practical sense true zero-g does not exist anywhere in the universe as there are always small, but nonetheless, measurable forces which can accelerate any massive body. For instance in low-Earth orbit, accelerations due to aerodynamic resistance in the tenuous outer atmosphere are on the order of $1 \times 10^{-6} g_0$ (from hence comes the term “microgravity”). This small drag acceleration provides some ersatz gravity, but there are also other forces present. Foremost of these are capillary forces.

Capillary forces are due to the cumulative effects of a large number of very short range molecular interactions and in a $1-g_0$ context are usually quite weak, relatively speaking. However, in a low-gravity environment other forces are so weak that the capillary forces becomes extraordinarily strong in a relative sense. In comparing the relative magnitudes of gravity and the capillary force we arrive at our figure of merit for assessing how wrong our fluid mechanical intuition is likely to be in a low-gravity context. This figure of merit is the Bond number dimensionless group

$$\text{Bo} \equiv \frac{gR^2\Delta\rho}{\gamma},$$

where g is the acceleration, R is the characteristic interfacial length scale, $\Delta\rho$ is the difference in densities across the interface (which simplifies to ρ , for large $\Delta\rho$, as in the case of a air-water interface), and where γ is the surface tension. In cases where Bo is small, a liquid is effectively in low-gravity regardless of the nominal local gravity level. Very small drops ($R < 1 \text{ mm}$), for instance, are in low-gravity for all intents and purposes and have nearly spherical shapes. Contrarily, for cases of large R in a space environment, such as with large diameter spacecraft propellant tanks then $\text{Bo} \gg 1$ even though the acceleration remains small. This is actually a quite useful result, for on the basis of dimensional similarity, it is possible to accurately simulate low-gravity fluid mechanics (say of large propellant tanks), even in small drop towers simply by scaling dimensionless groups like the Bond number.

As with capillary forces, electrostatic forces have a multitude of applications as substitutes for gravity. Electrohydrodynamic (EHD) body forces have been suggested to combat thermal stratification of propellants under low-g conditions where buoyancy induced natural convection is very small[blackmon collection 1965]. In this case electro-convection is an analog of natural convection due to a fluid temperature dependent dielectric permitivity gradient (as opposed to a fluid density gradient), in the presence of a body force field: the electric field. The study also suggested applications in cryogenic tank vent screening, and in reducing heat transfer to cryogenic propellants (and thus boiloff losses) by dielectrophoretically positioning ullage vapors around the tank walls as a thermal barrier. EHD forces have been studied for enhancing boiling heat transfer by promotion of bubble detachment and prevention of dryout, again as an ersatz buoyancy[snyder dielectrophoresis 2001][di marco influence 2003][marco use 2012]. EHD heat pipes, which substitute an electrode structure for the capillary wicking structure of a conventional thermocapillary heat pipe can evade the wicking limit[jones electrohydrodynamic 1973]. These are restricted to the use of insulating dielectric liquids, which usually have relatively low thermal conductivity, but are highly robust against dryout, support active flow control, and have low viscous losses. Dielectrophoretic settling of cryogenic propellants, in both total and partial communication Propellant Management Device (PMD) configurations, has been studied analytically in both static[hurwitz electrohydrodynamic 1966] and dynamic cases[koval dynamics 1967], and in drop tower experiments[fax dielectrophoretic 1969]. EHD forces have also been applied to the low-g slosh baffling problem[boretz orbital 1970][petra and studied extensively for the mitigation of vapor pullthrough during tank draining, and concomittent minimization of propellant residuals at burnout, in a series of experiments at the NASA Lewis (now Glenn) Research Center 2.2 s drop tower facility[berenyi dielectrophoretic 1970].

1.1 Spontaneous Drop Jump

Low-gravity phase separation, droplet dynamics, and the dynamics and applications of the so-called spontaneous droplet jump, is an active area of study at the Portland State University Dryden Drop Tower laboratory (DDT). When a nonwetting, gravity dominated sessile droplet (e.g. a puddle), which is initially at rest on a surface in the Cassie-Baxter state suddenly undergoes a large step reduction in $\Delta\theta$ it will spontaneously jump away from the surface. The Cassie-Baxter state, sometimes also known as the Fakir state, is a metastable heterogenously non-wetting state on a textured surface

characterized by the existance of a vapor-layer which seperates roughness features of the surface from the bottom of the droplet. The spontaneous drop jump was first observed experimentally in the Soviet Union by Kirko *et al.*[**kirko·phenomenon·1970**] in 1970 for drops of mercury in hydrochloric acid, and later by Wollman *et al.* in 2016 for water drops in a set of experiments conducted using drop towers[**wollman·more·2016**]. The kinetic energy of the jump is supplied by the defect in free surface energy as the new minimum energy surface equilibrium has approximately constant curvature. If the energy losses by viscous and contact line dynamics are neglected, the available kinetic energy is approximated by

$$KE_2 = SE_2 - SE_1 = [(\gamma A)_{gl} + (\gamma A)_{sg}]_2 - [(\gamma A)_{ls} + (\gamma A)_{gl} + (\gamma A)_{sg}]_1,$$

where KE and SE are the kinetic and surface energies, A is the surface area, the subscripts $_1$ and $_2$ denote the intial $1-g_0$, and low-g states, and the subscripts gl , sg , and ls denote the gas-liquid, solid-gas and liquid-solid interfaces repectively. The motive force is due to the inertia of internal flows which occur as the interface deflects under the suddenly lessened $\mathbb{B}o$. The characteristic time scale of the rolling up scales as $t_j \sim (\rho V_d/\sigma)^{1/2}$ [**attari·puddle·2016**], which resembles the contact time, $\tau \approx 2.6(\rho R_d^3/\sigma)^{1/2}$ presented by Richard *et al.* in 2002 for the related problem of drops impacting hydrophobic surfaces in $1-g_0$ [**richard·surface·2002**]. For drops with radial symmetry and sufficiently high initial $\mathbb{B}o$, inward radial capillary waves coalesce at the axis, leading to geysering and creation of satellite droplets by the Rayleigh-Plateau breakup of the geyser. In the case of smaller jumping drops the capillary waves are gradually damped by viscous forces. A time-lapsed composite photograph of spontaneous drop jump can be seen in Figure 1.1.

The physics of these relatively massive drops (far beyond the $1-g_0$ millimetric capillary length scale) at once utterly defy terrestrial expectations about the ways in which liquid ‘should’ behave, and also are of critical practical importance to space systems design where examples of such large capillary length scale multiphase flows are commonplace.

1.2 Drop Electro-Bounce

During the ‘rolling-up’ of drops under ideal conditions, the spontaneous jump phenomenon is governed by a balance of inertia and surface tension forces, and once aloft the drop motion is nominally in a regime of pure drag. However, other forces can again come into play.



Figure 1.1: The trajectory of a 0.2 mL spontaneous drop jump is captured in a composite image over a period ~ 0.67 s at 120 fps.

We have observed jumped drops to occasionally decelerate and return to the superhydrophobic surface, rebounding multiple times in the fashion of rigid bodies bouncing under $1-g_0$. The forces at work in such situations are presumably electrostatic in origin. Though this was an unintended effect during our work on spontaneous drop jump, the phenomenon is interesting itself. There is a certain irony to this typical failure of low-gravity intuition, where relatively tiny electrostatic forces have become suddenly large in the absence of gravity leading to unintentional experimental results, being as we are experienced low-gravity researchers who perhaps should know better. A time-lapsed composite image showing an example of the phenomenon is shown in Figure 1.2.

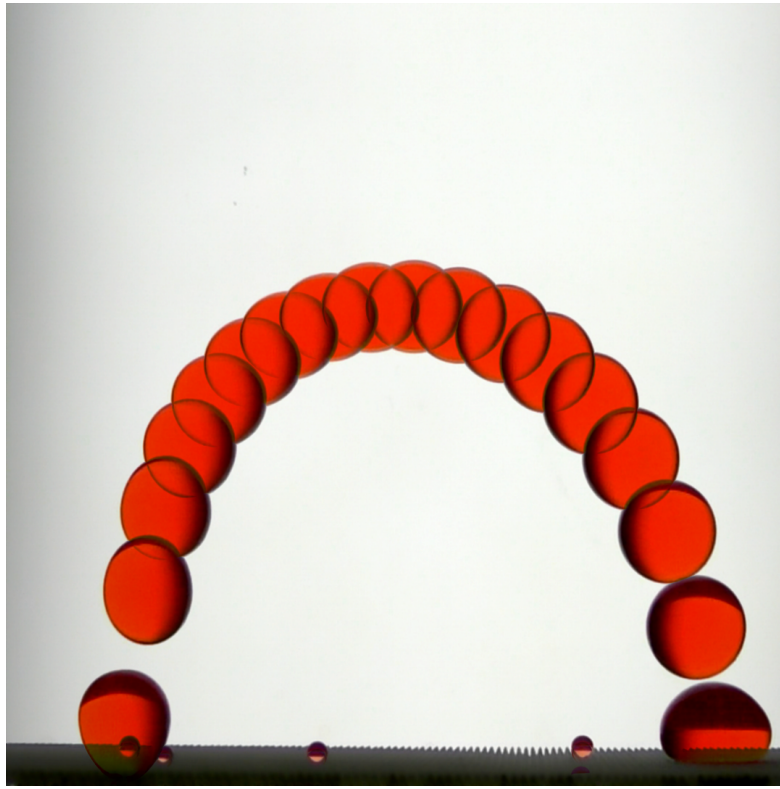


Figure 1.2: The trajectory of a 0.5 mL drop is captured in a composite image over a single bounce period (~ 1.25 s). The surface potential of the superhydrophobic dielectric in this example is $\varphi_s = 1.25 \pm 0.41$ kV.

This “electro-bounce” phenomenon is the subject of this thesis. We begin with some preliminary observations of the phenomenon:

- Observed maximum drop (de-)accelerations are on the order of ~ 30 cm/s² for a range of drop volumes $0.03 \lesssim V_d \lesssim 0.5$ mL.
- The drops are attracted to regions of high electric field. The horizontal (surface plane parallel) components of the drop trajectory usually oscillate about their initial position during the experiment (except in cases of nearly pure 1-D vertical translation). For especially small drops close to the spontaneous drop jump limit ($V_d \sim 0.01$ mL) the drops do not jump, but translate across the surface in a rolling regime until either they reach a local maximum of the electric field, or until their motion is sufficiently damped by contact line hysteresis that pinning arrests their motion.
- The drops appear to have net free charge. In cases of multiple simul-

taneous drop jumps the drops repel each other as they bounce or roll in orbital motion around regions of high field.

- The magnitude of the drop trajectory maxima (apoapses) appear to be related to the drop volume, which affects their mass, and initial jump velocity, and thence their inertia, and to the electric field strength.

There are several possible origins of the electric charge which are ultimately responsible for this phenomenon. It is well known that water acquires positive free charge when in contact with certain polymers, especially polytetrafluoroethylene (PTFE)[**langmuir·surface·1938**], through a process called contact charging. PTFE, on the other hand, tends to readily acquire negative charge by contact with water. The superhydrophobic surfaces used in the spontaneous drop jump experiments have thin (nanometric) PTFE coatings, and we observe that it is extremely easy to produce significant surface potentials, $\varphi_s \sim 100\text{-}500$ V, by simply flowing streams of distilled water over them. A study of this water on PTFE contact charging phenomenon was conducted by Yatsuzuka *et al.*[**yatsuzuka·electrification·1994**], who suggest that this process results from formation of an electrical double layer driven by selective adsorption of (OH^-) ions at the polymer surface; other recent work strongly supports this hypothesis[**beattie·intrinsic·2006**][**strazdaite·water·2015**]. Yatsuzuka *et al.* also found that the specific charge on the drops in contact with the surface depends on their both surface velocity and conductivity. The contact charging mechanism is the most likely accidental source of charge on the superhydrophobic surfaces used in our work. Given the large roughness, or the ratio of projected to actual surface area, of the superhydrophobic surfaces used in the experiment, and given that the drops are initially in a Cassie-Baxter state, a somewhat electrically resistive air layer is maintained that reduces grounding of the drops despite the large potential difference between them and the surface charges. If this electrostatic potential is greater than the release of surface energy under the sudden change in \mathbb{B}_0 , in the form of the drop kinetic energy, we expect that the drop will return to an equilibrium state on the charged surface which minimizes the potential.

The source of the net free charge on the drops is another issue. The drop charge could of course also be due to the contact charging mechanism mentioned previously. For instance, in a 1996 paper, NASA flight engineer Don Pettit discusses the problem of low-gravity flow induced charging of liquids, resulting ultimately from contact charging phenomenon[**pettit·donald·flow·????**]. Another mechanism for the drop charge is field-induced charging. Field-induced charging occurs due to physical breakup of a conductor having a field-induced dipole (e.g a physical separation of charge). In our work this might occur when a drop is deposited on the charged surface by a grounded

syringe. The metal syringe needle tip, and the liquid in the syringe itself are essentially a ground connection which is broken when the syringe is suddenly removed in the presence of an external electric field. Field-induced charging is at work in the famous Kelvin thunderstorm, and is applied in inkjet, and electrospray technologies, where in each case the breakup is by the Rayleigh-Plateau instability. Notably, in Pettit's aforementioned discussion of contact charging of liquids in low-g, he remarks on accidental electrostatic 'hula-ing' of silicone oil drops when ejected from a syringe in the vicinity of a highly-charged polymer surface during an experiment conducted aboard STS-5 by mission specialist Joseph Allen[**pettit·donald·flow·?????**]. Depending on the (highly-variable) electrical conductivity of the silicone oil, and the material of the syringe used in the experiment, the charge could arise just as easily by field-induction as by contact charging. Relatedly, in a series of informal, and somewhat whimsical experiments, Pettit himself electrostatically orbited small water drops around a triboelectrically charged PTFE knitting needle while aboard ISS during expedition 30/31[**stevenson·electrostatic·2015**]. Again, in this case, the drop charge is likely field-induced.

1.3 Applications

This study of the drop electro-bounce phenomenon may have results which can be extended to useful applications in a space environment. External surfaces of spacecraft tend to become charged with time due to the space environment itself. Surface charging largely occurs due to low energy electrons (3-50 keV) which do not penetrate the surface of the spacecraft external structure[**czeplia·charging·1997**]. The ultimate sources of these charges are trapped charged particles of the van Allen radiation belts, galactic cosmic rays, and the solar wind. This deposited charge accumulates and can lead to significant potential differences between different parts of a spacecraft, sometime leading to breakdown and discharge, called Paschen discharge. Deep dielectric charging occurs when higher energy charged particles penetrate the surface of a dielectric material, which can also lead to large potential differences if the dielectric leakage is lower than the external charging rate. In a fluid mechanical context, this accumulated charge could be problematic during any multiphase venting process, as might be expected to occur during autonomous satellite servicing refueling operations, or during boil-off venting of cryogens stored over long periods in a space environment (as in many crewed Mars mission scenarios, or in cryogenic propellant depot operations). Such venting, if occurring in a region of strong field, will also tend to produce a stream of charged drops, which will be decelerated by the field,

causing their eventual return, impacting and potentially contaminating the spacecraft surfaces.

As previously noted, robust phase separation is critical to high reliability multiphase systems used in thermal control and life support. Active (but solid-state) phase separation for life support multiphase flows, especially high void-fraction droplet-disperse flows is a possible application of this work. Such flows are encountered in dish washing, laundry, waste solids drying, food processing, the Sabatier CO₂ reaction, and possibly in vapor-compression cycle condensers. Phase separation for other disperse droplet flows include electrostatic droplet separators for high-efficiency Rankine-cycle turbines, which require a droplet-free vapor phase entering the turbine, but where conventional superheat approaches comes with severe mass penalties[**unterberg'zero'1962**], or more speculatively, in high temperature liquid droplet radiators with electrostatic collection[**white'liquid'1987**]. Removal of satellite droplets produced during pipetting in wet-lab research outside of a glovebox environment aboard ISS has also been recently suggested as a application of the work [private communication, NASA JSC, E. Unger, 2017]. Drops can become spontaneously charged by contact with standard micropipette tips[**choi'spontaneous'2013**], and this free charge can possibly be leveraged for the purposes of phase separation in low-gravity.

1.4 Overview of this Thesis

In this thesis we develop, and partly validate a simple model to aid in design of future electrostatic disperse drop phase separators. To this end the work encompasses:

1. A mathematical model of the drop electro-bounce, its scale analysis, asymptotic estimates for drop apoapses and times-of-flight.
2. The results of controlled experiments, where the effect of key independent variables drop volume V_d , and dielectric surface charge density σ , on drop trajectories is tested.

Chapter 2

Theory

2.1 Forces and the Equation of Motion

In this section we develop a simple, 1-dimensional model of the dynamics of drops dominated by electrostatic forces. We treat a drop as a particle with radius R_d , which translates vertically along the central axis of a charged dielectric square sheet substrate with initial velocity U_0 . The equation of motion for this system is given by,

$$my'' = -\mathbf{F}_D - \mathbf{F}_E, \quad (2.1)$$

subject to

$$y(0) = R_d, \quad \text{and} \quad y'(0) = U_0, \quad (2.2)$$

where m is the drop mass, $y'' = \frac{d^2y}{dt^2}$ is the drop acceleration, \mathbf{F}_D is the drag force which always opposes motion, and \mathbf{F}_E is the electrostatic force. The assumed initial conditions are such that, when \mathbb{B}_0 is suddenly reduced at the start of the drop tower free-fall period, the drop jumps with instantaneous initial velocity U_0 from its $1-g_0$ resting position with fixed radius R_d at $t = 0$. We now define models for each of the forces in this equation.

For the intermediate range of Reynolds numbers $1 \leq \mathbb{R}_e \equiv \frac{2UR_d}{\nu} \leq 5000$ observed in our experiments the force of drag acting on the drop may be quadratic such that,

$$\mathbf{F}_D = \frac{1}{2}C_D\rho Ay'^2,$$

where C_D is the drag coefficient, ρ is the density of the air host fluid, and A is the frontal projected area of the drop. For this range of Reynolds numbers the drag coefficient may be approximated by the well known Abraham

correlation[**abraham**·**functional**·**1970**],

$$C_D = \frac{24}{9.06^2} \left(1 + \frac{9.06}{\sqrt{\text{Re}}} \right)^2.$$

Modeling the electrostatic force is more involved, but we begin with the standard electrohydrodynamic (EHD) approximation[**saville**·**electrohydrodynamics**:**1997**]. Under a DC electric field, we assume that the real part of the dielectric permittivity ϵ , $\text{Re}\langle\epsilon\rangle \approx \text{constant}$. We also assume that electric currents are small enough that the effects of magnetic fields can be neglected. The validity of this assumption rests on the characteristic time scale for electrical phenomena $\tau_e = \epsilon/\sigma_e \ll 1$, where τ_e is the ratio of absolute dielectric permittivity $\epsilon = \kappa\epsilon_0$, to conductivity σ_e , of the medium, κ is the relative dielectric permittivity, and ϵ_0 is the vacuum permittivity. This characteristic time τ_e is also known as the relaxation time, and is a measure of how quickly the polarization of a dielectric responds to a change in electric field. Given the conductivity, and permittivity in the limiting case of extremely-pure water ($\epsilon \sim 80$, $\sigma_e = 18.2 \times 10^6 \Omega\text{cm}$) [**yatsuzuka**·**electrification**·**1994**], we estimate $\tau_e \approx 4 \times 10^{-6} \text{ s}$. The relaxation time for the common distilled water that is actually used in the drop experiments is undoubtedly shorter due to the presence of solvated ions. Neglecting the effects of an electric double layer on hydration of ions in the water or the ambient atmosphere due to the relatively massive size of the drops studied, then the assumption of small relaxation time further implies that the free charge present in the drops will remain approximately constant during the typical time interval of a low-gravity experiment.

Supposing that electrical forces acting on free charges and dipoles in a fluid are transferred directly to the fluid itself, the overall electrical body force will be the divergence of the Maxwell stress tensor τ_m ,

$$\mathbf{F}_E = \nabla \cdot \tau_m = \nabla \cdot \left(\epsilon \mathbf{E} \mathbf{E} - \frac{1}{2} \epsilon \mathbf{E} \cdot \mathbf{E} \delta \right),$$

where \mathbf{F}_E is the electric body force per unit volume, and δ is the Dirac delta function. The product of the electric field vectors is the dyadic product.

The Korteweg-Helmholtz volumetric force density formulation of the Maxwell stress tensor is usually expressed as[**melcher**·**continuum**·**????**]

$$\mathbf{F}_E = \rho_f \mathbf{E} + \frac{1}{2} |E|^2 \nabla \epsilon - \nabla \left(\frac{1}{2} \rho \left(\frac{\partial \epsilon}{\partial \rho} \right)_T |E|^2 \right). \quad (2.3)$$

The first term on the right hand side this expression, is the well known Coulombic force or electrophoretic force, which arises from the presence of

free charge in an external electric field. We expect this term to dominate the electric force in a DC field. The second term is the force arising from polarization stresses due to a nonuniform field acting across a gradient in permittivity. This force is widely termed the dielectrophoretic (DEP) force. The third term describes forces due to electrostriction. It has been noted by Melcher and Hurwitz that the electrostriction term is the gradient of a scalar and can thus be canonically lumped together with the hydrostatic pressure for incompressible fluids[hurwitz'electrohydrodynamic'1966]. We neglect it in our analysis.

It is common to approximate the polarization stress by idealizing the drop as a simple dipole using the effective dipole moment method first described by Pohl in 1958[pohl'effects'1958]. This approach has since been related back to the force density by the volumetric integration of the force density with the substitution of a Taylor series expansion of \mathbf{E} in the limit of a small radial gradient of the field within the dielectric sphere[wang'general'1997]. The DEP force is related to the induced or permanent dipole moment of polarizable media which has a tendency to align the dipole with the electric field. If there is a gradient in the field then for a finite separation of charge, one end of the dipole will feel a stronger electric field than the other resulting in a net force. Whether the force is positive or negative in the direction of the electric field gradient depends on the difference of dielectric permittivities between the fluids, rather than on the polarity of \mathbf{E} . In principle an external electric field will tend to induce a dipole in a dielectric material, but if the field is spatially uniform there is no gradient in the field and the forces felt by the dipoles are symmetric with no net force. The dipole moment μ , of a spherical linear-dielectric particle immersed in a dielectric medium is given by

$$\mu = V_d \mathbf{P} = \frac{4}{3}\pi R_d^3 \mathbf{P}, \quad (2.4)$$

where $\mathbf{P} = (\kappa_1 - 1)\epsilon_0 \mathbf{E} = \chi_e \epsilon_0 \mathbf{E}$ is the polarization moment, and R_d is the particle radius, $\kappa_1 = \frac{\epsilon_1}{\epsilon_0}$ is the relative dielectric constant of the air host fluid, $\chi_e = \kappa_1 - 1$ is the electric susceptibility of the host fluid. The force felt by the dipole is

$$\begin{aligned} \mathbf{F}_{DEP} &= (\mathbf{P}_e \cdot \nabla) \mathbf{E} \\ &= 2\pi R_d^3 \epsilon K \nabla E^2, \end{aligned} \quad (2.5)$$

where $\mathbf{P}_e = (\kappa_2 - \kappa_1)\epsilon_0 \mathbf{E}$ is the excess polarization, and κ_2 is the relative dielectric constant of the water particle. Here it is convenient to use the simplifying shorthand $K = \frac{\kappa_2 - \kappa_1}{\kappa_2 + 2\kappa_1}$, known as the Clausius-Mossotti factor. In cases where $K < 0$, or $K > 0$ the particle will be either repelled or attracted to regions of strong field. In our experiment, choosing the relative

dielectric constants $\kappa_1 \approx 1$ and $\kappa_2 \approx 80$, $K \approx 0.96$. It is important to note that the equivalent dipole approximation critically requires an assumption of small physical scale of the particle relative to the length scale of nonuniformity of the field, which in this case we take to be the length of the charged superhydrophobic surface, $L = 25$ mm $\gg R_d \approx 2$ mm.

When the drop is close to the dielectric surface, the free charge on the drop will tend to induce polarization of the dielectric which perturbs the electric field. The polarization bound charge in the dielectric will be of the opposite sign of the free drop charge and thus there will be a force of attraction. This so-called image force is a correction to the Coulomb force due to the external electric field only, and can be found by a Green's Function solution to Laplace's equation for the electric field called the 'method of images'[david j. griffiths introduction 1999]. This resulting image force \mathbf{F}_I , is given by

$$\mathbf{F}_I = \frac{kq^2}{16\pi\epsilon_0} y^{-2} \hat{\mathbf{j}}, \quad (2.6)$$

where the factor k is a function of the dielectric surface susceptibility $k = \frac{\chi_e}{\chi_e + 2}$, and $\hat{\mathbf{j}}$ is a unit vector normal to the dielectric surface.

By substituting Equations 2.5, and 2.6 into 2.3 we have

$$\begin{aligned} \mathbf{F}_E &= q\mathbf{E} + \mathbf{F}_{DEP} + \mathbf{F}_I \\ &= q\mathbf{E} + \frac{kq^2}{16\pi\epsilon_0} y^{-2} \hat{\mathbf{j}} + 2\pi R_d^3 \epsilon K \nabla E^2, \end{aligned}$$

and the 1-D governing equation becomes

$$my'' = -\frac{1}{2} C_D \rho A y'^2 - qE - \frac{kq^2}{16\pi\epsilon_0} y^{-2} - 2\pi R_d^3 \kappa_1 \epsilon_0 K \nabla E^2, \quad (2.7)$$

subject to

$$y(0) = R, \quad \text{and} \quad y'(0) = U_0. \quad (2.8)$$

By comparing DEP and Coulombic terms in Equation 2.7, we note that a condition to neglect the DEP force is

$$\frac{\kappa_2 \epsilon_0 K R_d^2 E_0}{q} \ll 1$$

As this condition likely prevails in our experiments we henceforth neglect the DEP force. There is some physical intuition to support this conclusion as well. The dielectric displacement $\mathbf{D} = \kappa \epsilon_0 \mathbf{E}$ of a water drop in air is very high due to its large relative dielectric constant. This implies that the field strength within the drop is about 80 times smaller than in the surrounding

medium (which is essentially the same as a vacuum from a dielectric standpoint), thus it is not particularly inaccurate to model the dielectric volume of a drop as an equipotential conductive shell, with zero field in its interior. As an aside, in treating the drop as an ideal conductor we note that in our specific case the electrostatic force is not a body force *per se* as the electric field is acting on charges on the surface of the conductor.

2.2 The Electric Field

If we consider the charged dielectric surface of our experiments to be a square sheet of charge lying in the xz -plane with width L , the symmetry of the problem happily lets us obtain the y -component of the electric field \mathbf{E} by direct integration. In particular, it is easy to construct the electric field due to a finite plane of charge by superposition of the electric fields of a series of line charges. By symmetry, the electric field points along the y -axis; for a point along the y -axis the position vector is $\mathbf{r} = (x^2 + y^2)^{1/2} \hat{\mathbf{r}}$ to the center of a line charge in the xz -plane. The y -component of $d\mathbf{E}$ is found by $dE_r = dE_y \cos \theta = dE_y y/r$, where θ is the angle made between the y -axis and the position vector \mathbf{r} . If the charge in a line element, dx is $\sigma L dx$, where σ is the average surface charge density, the electric field of a line charge is given by [david j. griffiths introduction 1999]

$$dE_r = \frac{k\sigma L dx}{4\pi\epsilon_0 r \sqrt{r^2 + L^2/4}}.$$

The y -component of the electric field E_y , hence E , is then

$$E = \frac{\sigma Ly}{4\pi\epsilon_0} \int_{-L/2}^{L/2} \frac{1}{(y^2 + x^2) \sqrt{y^2 + x^2 + L^2/4}} dx.$$

With some substitutions the above can be integrated to obtain an expression for the electric field in terms of y ,

$$E = \frac{\sigma}{\pi\epsilon_0} \tan^{-1} \left(\frac{L^2}{y\sqrt{2L^2 + 4y^2}} \right). \quad (2.9)$$

We note that this model of the electric field is valid when $R_d \ll L$, which will be true for cases of small drops ‘far’ from the dielectric surface. For accurate models of the field in the case $R_d/L \sim \mathcal{O}(1)$ we likely need to solve Laplace’s equation for the electric potential φ ,

$$-\nabla^2 \varphi = 0,$$

using numerical methods.

By taking Taylor series expansions in large and small limits we can intuit a bit about the behavior of this field. In the limit $y/L \ll 1$ Equation 2.9 reduces to

$$E \approx \frac{\sigma}{4\pi\epsilon_0} = E_0, , \quad (2.10)$$

where E_0 is the characteristic electric field given by $E_0 = \frac{\sigma}{4\pi\epsilon_0}$. This field is constant and equivalent to the electric field due to an infinite plane of charge. In the limit of $y/L \gg 1$, Equation 2.9 reduces to the familiar electric field due to a point charge

$$E \approx L^2 E_0 y^{-2}. \quad (2.11)$$

Both regimes given by Equations 2.10, 2.11 can be clearly seen in Figure 2.1.

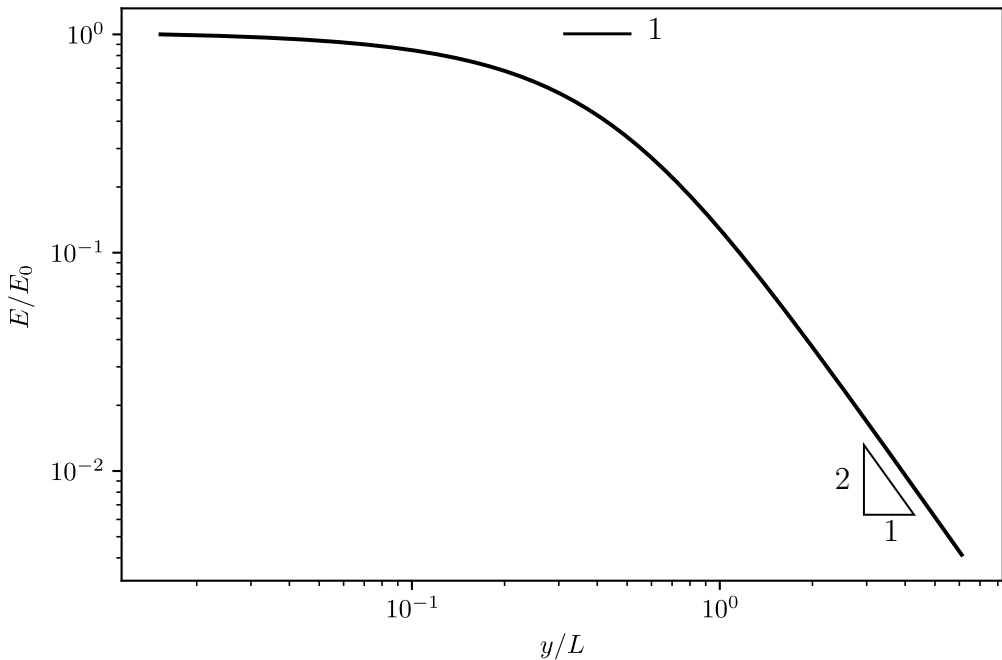


Figure 2.1: A log-log plot of the magnitude of the dimensionless electric field E .

2.3 Scaling

For small DEP forces, the equation of motion, Equation 2.7, is non-linear, non-homogeneous and must be solved numerically. Nevertheless we are curious if we can obtain approximate solutions to the equation analytically using perturbation methods. This is aided by non-dimensionalizing the governing equations, forming dimensionless groups, and determining whether any are particularly small or large, and whether any fortuitous opportunities for simplification appear. Introducing the scaled variables

$$t^* = \frac{t}{t_c}, \quad y^* = \frac{y}{y_c}, \quad (2.12)$$

where y_c and t_c are characteristic length and time scales respectively, and using the coordinate transformation $y(0) - R = 0$, the governing equation becomes

$$y^{*''} = -\frac{1}{2} \frac{C_D \rho A y_c}{m} y^{*'^2} - \frac{q E_0 t_c^2}{m y_c} E^*(y^*) - \frac{k q^2 t_c^2}{16 \pi \epsilon_0 R^2 m y_c} \left(\frac{y_c}{R} y^* + 1 \right)^{-2}, \quad (2.13)$$

subject to

$$y^*(0) = 0, \quad \text{and} \quad y^{*'}(0) = \frac{U_0 t_c}{y_c}.$$

We note the existence of several dimensionless groups

$$\Pi_1 = \frac{C_D \rho A y_c}{2m}, \quad \Pi_2 = \frac{q E_0 t_c^2}{m y_c}, \quad \Pi_3 = \frac{k q^2 t_c^2}{16 \pi \epsilon_0 R^2 m y_c}, \quad \Pi_4 = \frac{y_c}{R}, \quad \Pi_5 = \frac{U_0 t_c}{y_c},$$

such that Equation 2.13 becomes

$$y^{*''} = -\Pi_1 y^{*'^2} - \Pi_2 E^*(y^*) - \Pi_3 (\Pi_4 y^* + 1)^{-2}, \quad (2.14)$$

subject to

$$y^*(0) = 0, \quad \text{and} \quad y^{*'}(0) = \Pi_5.$$

2.3.1 Inertial Electro-Image Limit

In the limit of small y and t we expect inertia to scale with Coulombic and image forces. In this limit we can approximate the electric field as the constant E_0 . One possible characteristic length scale is $y_c \sim R_d$, however this scale is overly restrictive with respect to time. With $y_c \sim U_0 t_c$ and picking

t_c such that the Coulombic force $\mathbf{\Pi}_3 \sim \mathcal{O}(1)$, the intrinsic scales are found such that

$$t_c \sim \frac{mU_0}{qE_0}, \quad \text{and} \quad y_c \sim \frac{mU_0^2}{qE_0}.$$

With these scales the governing equation 2.14 becomes

$$y^{*''} = -1 - \mathbb{Ig} (\mathbb{E}uy^* + 1)^{-2}, \quad (2.15)$$

subject to

$$y^*(0) = 0, \quad \text{and} \quad y^{*'}(0) = 1.$$

with

$$\mathbb{Ig} \equiv \frac{kq}{16\pi\epsilon_0 R_d^2 E_0} = \mathbf{\Pi}_3, \quad \mathbb{E}u \equiv \frac{mU_0^2}{qE_0 R_d} = \mathbf{\Pi}_4,$$

where the Image number \mathbb{Ig} is the ratio of image forces to the Coulombic force of the unperturbed field, and the electrostatic Euler number $\mathbb{E}u$ is the ratio of inertia to electrostatic force. With these dimensionless groups the intrinsic scales become

$$t_c = \mathbb{E}u \frac{R_d}{U_0}, \quad \text{and} \quad y_c = \mathbb{E}u R_d.$$

2.3.2 Inertial Electro-Viscous Limit

In the limit of large y and t we expect drop inertia to balance Coulombic force and drag. In this limit we approximate the electric field as $E \approx y_c^2 E_0 y^{-2}$. In this case there are several obvious possible choices of scales:

1. $y_c \sim U_0 t_c$, and $\mathbf{\Pi}_3 \sim \mathcal{O}(1)$.
2. $y_c \sim L$, $t_c \sim \frac{L}{U_0}$ (making Equation 2.13 singular).
3. $y_c \sim L$, $t_c \sim \left(\frac{Lm}{qE_0}\right)^{1/2}$.
4. $y_c \sim L$, and $\mathbf{\Pi}_3 \sim \mathcal{O}(1)$.

We choose the Case 1 scaling for its combination of physical simplicity, few $\mathbf{\Pi}$ terms, and homogeneous initial conditions. The intrinsic scales for this case are given by

$$t_c \sim \frac{R_d^2}{L^2} \frac{4\pi m U_0}{qE_0}, \quad \text{and} \quad y_c \sim \frac{R_d^2}{L^2} \frac{4\pi m U_0^2}{qE_0}.$$

With this scaling the non-dimensional governing equation is

$$y^{*''} = -\mathbb{D}g B \mathbb{E}u y^{*'^2} - (B \mathbb{E}u y^* + 1)^{-2}, \quad (2.16)$$

subject to

$$y^*(0) = 0, \quad \text{and} \quad y^{*'}(0) = 1,$$

where we call $\mathbb{D}g$ the drag number $\mathbb{D}g \equiv \frac{C_D \rho_a}{\rho_l} = \Pi_1 B^{-1} \mathbb{E}u^{-1}$, and $B = 4\pi \frac{R_d^2}{L^2}$ is a dimensionless ratio of length scales.

2.4 Asymptotic Estimates

2.4.1 Inertial Electro-Image Limit

The alternate scalings of the equation of motion given by Equations 2.15, and 2.16 are weakly non-linear differential equations in the sense that they reduce to linear equations as the parameter $\mathbb{E}u \rightarrow 0$. If we take $\mathbb{E}u$ to be a small parameter we can find an asymptotic approximation to the solution of the non-linear equation by means of a regular perturbation. In this case we use the naive expansion

$$y^*(t^*) \sim y_0^*(t^*) + \mathbb{E}u y_1^*(t^*) + \mathbb{E}u^2 y_2^*(t^*) \dots \mathbb{E}u^n y_n^*(t^*). \quad (2.17)$$

By substitution of the expansion 2.17 and its derivatives into 2.14, and equating terms by order we first find the $\mathcal{O}(1)$ unperturbed solution

$$y_0^*(t^*) = t^* + \frac{t^{*2}}{2} (-1 - \mathbb{I}g).$$

Looking at this solution it is evident that if $\mathbb{I}g = 0$, the solution is the classical kinematic equation for projectile motion without drag under constant gravity g_0 . Continuing on with this procedure we find, after some tedious computations documented in the project repository for this thesis [schmidt·droplet·electro-bounce]:² the $\mathcal{O}(\mathbb{E}u^5)$ order accurate solution, truncated to $\mathcal{O}(\mathbb{E}u^2)$ below.

$$\begin{aligned} y^*(t^*) &= t^* + \frac{t^{*2}}{2} (-1 - \mathbb{I}g) + \mathbb{E}u \left(\frac{\mathbb{I}gt^{*3}}{3} + \frac{\mathbb{I}gt^{*4}}{12} (-1 - \mathbb{I}g) \right) \\ &\quad + \mathbb{E}u^2 \left(-\frac{\mathbb{I}gt^{*4}}{4} + \frac{\mathbb{I}gt^{*5}}{60} (9 + 11\mathbb{I}g) + \frac{\mathbb{I}gt^{*6}}{360} (-9 - 20\mathbb{I}g - 11\mathbb{I}g^2) \right) + \mathcal{O}(\mathbb{E}u^3). \end{aligned} \quad (2.18)$$

We plot the approximate short-time scaled solution Equation 2.18 with varying values of $\mathbb{I}g$ in Figure 2.3. These plots show a trend of decreasing time-of-flight t_f , which is the time for the drop to return to the origin, or complete a single ‘bounce’, and height at apoapse with increasing values of $\mathbb{I}g$. When

$\mathbb{I}g = 1$, t_f is exactly half of characteristic time scale in this regime. In the limit of small $\mathbb{E}u$ the trajectories collapse to the $\mathcal{O}(1)$ solution regardless of the Image number. In principle there is some coupling between $\mathbb{E}u$ and $\mathbb{I}g$; notably this relationship does not depend on the electric field E_0 but on a charge to mass ratio. The effect of contact line hysteresis on the initial jump velocity U_0 will also tend to independently decohere the natural covariance between these parameters.

2.4.2 Inertial Electro-Viscous Limit

By similar arguments we find an asymptotic estimate of the trajectory in the long-time regime. The approximate solution is

$$\begin{aligned} y^*(t^*) &= t^* - \frac{t^{*2}}{2} + B\mathbb{E}u \left(\frac{t^{*3}}{3} (1 + \mathbb{D}g) + \frac{t^{*4}}{12} (-1 - \mathbb{D}g) - \frac{\mathbb{D}gt^{*2}}{2} \right) \\ &\quad + B^2\mathbb{E}u^2 \left(\frac{t^{*4}}{12} (-3 - 3\mathbb{D}g - 4\mathbb{D}g^2) + \frac{t^{*5}}{60} (11 + 10\mathbb{D}g + 8\mathbb{D}g^2) \right. \\ &\quad \left. + \frac{t^{*6}}{360} (-11 - 10\mathbb{D}g - 8\mathbb{D}g^2) + \frac{\mathbb{D}g^2t^{*3}}{3} \right) + \mathcal{O}(B^3\mathbb{E}u^3). \end{aligned}$$

Trajectory for this solution are shown in Figure 2.4. If we assume a constant scale for the drag coefficient, $C_d \approx 0.5$, then $\mathbb{D}g$ is approximately a constant $\mathbb{D}g \approx 6 \times 10^{-4}$ in all of our experiments. Again, the trajectory seemingly reduces to the classical $\mathcal{O}(1)$ solution for small values of $\mathbb{E}u$. We also note that with $\mathbb{D}g = 6^{-4}$ the effect of drag is slight, appearing only as a slight correction to the higher order terms; the apoapse is nearly equal to half the characteristic length scale.

By again applying a regular perturbation to the asymptotic solution with the expansion

$$t^* \sim t_0^* + B\mathbb{E}u t_1^* + B^2\mathbb{E}u^2 t_2^* \dots B^n \mathbb{E}u^n t_n^*,$$

and solving for the roots at times when $y^* = 0$, we find an asymptotic estimate for the time-of-flight. The $\mathcal{O}(B^2\mathbb{E}u^2)$ accurate time-of-flight estimate is given by

$$t_f = 2 + B\mathbb{E}u \left(\frac{4}{3} - \frac{2\mathbb{D}g}{3} \right) + B^2\mathbb{E}u^2 \left(\frac{4}{5} - \frac{4\mathbb{D}g}{3} + \frac{2\mathbb{D}g^2}{5} \right) + \mathcal{O}(B^3\mathbb{E}u^3).$$

Substituting the experimental value of $\mathbb{D}g$ we find the time-of-flight estimate for water drops is

$$t_f = 2 + 1.333B\mathbb{E}u + 0.799B^2\mathbb{E}u^2 + \mathcal{O}(B^3\mathbb{E}u^3). \quad (2.19)$$

In Figure 2.5 we see the effect of increasing values of $B\mathbb{E}u$ on t_f . As $\mathbb{E}u$ grows to be no longer small, the time-of-flight grows rapidly, but this behavior appears to have an asymptote at a certain critical velocity; this is an electrostatic escape velocity U_e . We can find the escape velocity by solving a modified version of the equation of motion

$$mu' = -\frac{qE_0y_c^2}{y^2},$$

where $u = \frac{dy}{dt}$ is the drop velocity. Integrating between the respective limits we find

$$m \int_{U_0}^{u(y)} u du = -qE_0y_c^2 \int_{R_d}^y \frac{dy}{y^2},$$

which has the solution

$$u(y) = \pm U_0 \left[1 + \frac{2qE_0y_c^2}{mU_0^2} \left(\frac{1}{y} - \frac{1}{R_d} \right) \right]^{1/2}.$$

This equation has an asymptotic velocity, U_∞ at $y = \infty$ which is real provided

$$U_0 \geq U_e = y_c \sqrt{\frac{2qE_0}{mR_d}},$$

where U_e is the escape velocity and $U_\infty = \sqrt{U_0^2 - U_e^2}$. If $y_c = L$ the condition for the drops to escape the electric field is then given by

$$\frac{B}{8\pi} \mathbb{E}u > 1. \quad (2.20)$$

If the drop escapes the electric field it will have a residual velocity U_∞ , and will be in a regime of pure inertia \sim drag. The velocity will then decay as

$$u^*(t^*) = \frac{1}{t^* + 1},$$

with a characteristic time $t_c \sim \frac{2m}{C_D \rho A U_\infty}$, which is the halving time of the velocity.

2.5 Summary

The objective of this work is to understand the basic physics of the low-gravity drop bounce phenomenon to the point where we can make useful predictions of drop behavior for engineering purposes. To that end, in this chapter we have shown the following:

- We develop from first principles a simple 1-dimensional model of drop trajectories subject to Coulombic forces and drag under low-gravity. Drops are idealized as point charges. We find that polarization stresses are negligible, and that water drops can be modeled as ideal conductors under the conditions of our experiments.
- By scaling arguments we find characteristic length and time scales for both a short-times regime where inertia balances Coulombic force and forces due to image charges, and a long-times regime where inertia balances Coulombic force and drag. In both regimes a key dimensionless group appears: the electrostatic Euler number \mathbb{E}_u , which is a ratio of inertia to electrostatic force.
- The governing ODE is non-linear, but we find approximate analytic solutions for the drop trajectory and time of flight in both regimes by means of asymptotic expansions.
- We find a limiting initial velocity U_0 for which drop time of flight grows without bound. This electrostatic escape velocity is analogous to the gravitational escape velocity of a planet or other massive body.

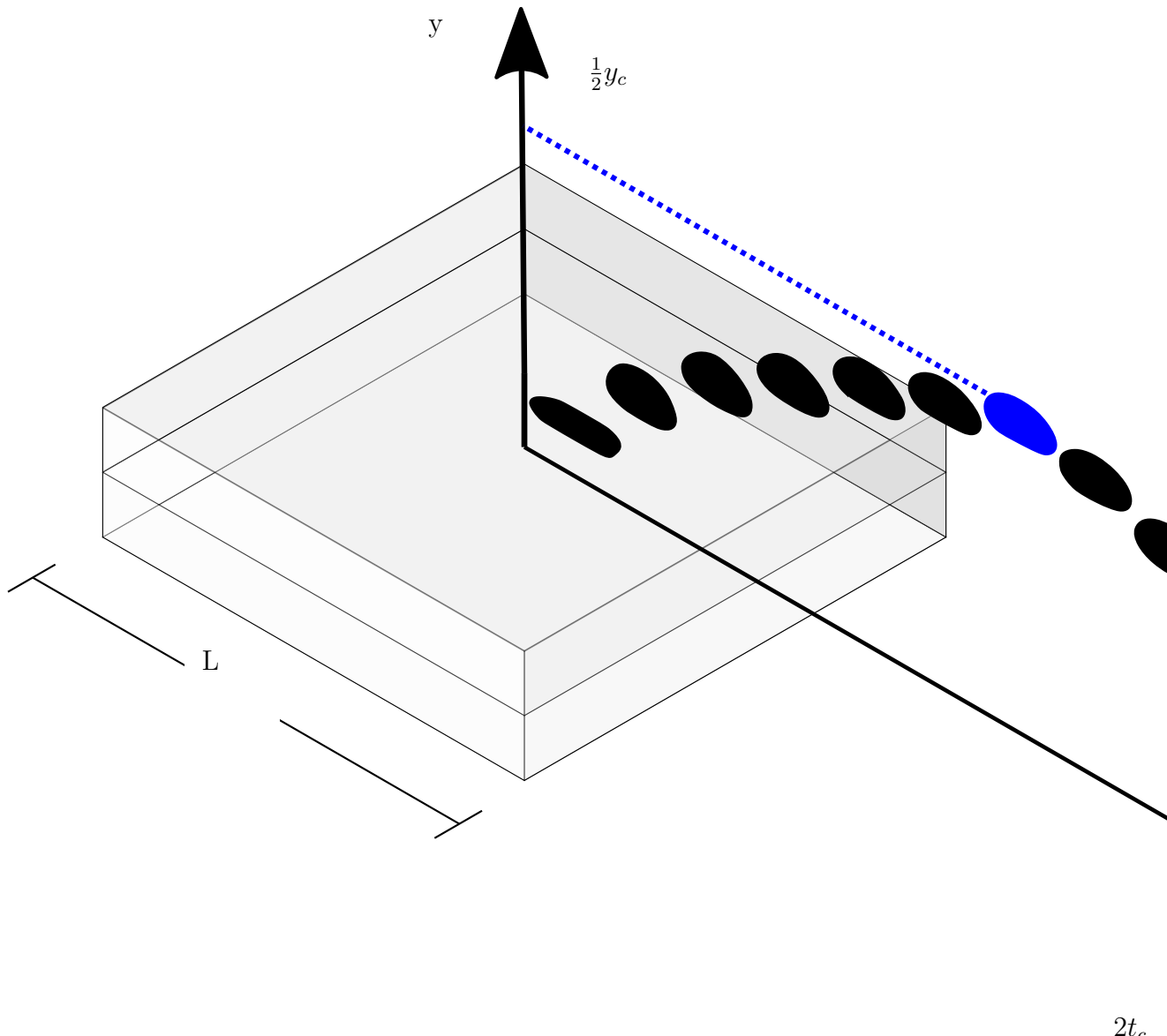


Figure 2.2: A schematic representation of a drop electro-bounce experiment with labeled characteristic time and length scales, t_c , y_c shown. Also shown are the dimensions of the superhydrophobic electret substrate.

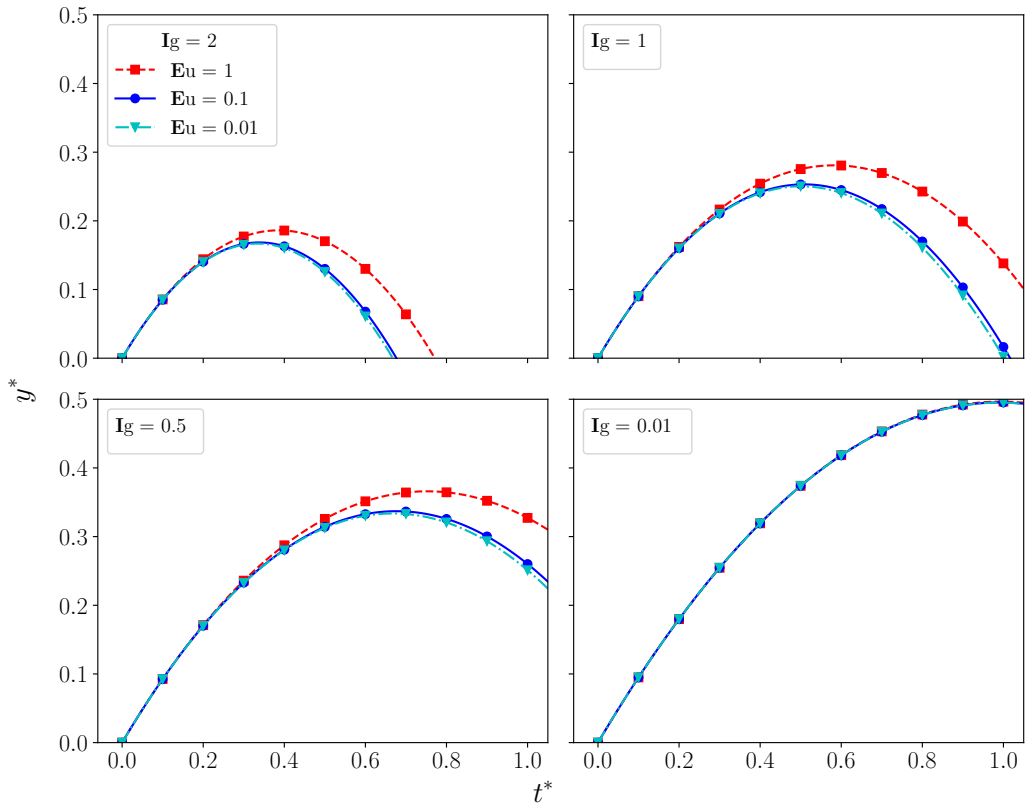


Figure 2.3: Short-time scaled drop trajectories for various values of Eu , Ig . The trajectory reduces to the classical $\mathcal{O}(1)$ solution for small values of Ig . It should be noted that despite what is implied by these plots Ig is not necessarily independent of Eu , as they share q , and E_0 as common factors, $U_0 \sim R_d^2$, and $m \sim R_d^3$.

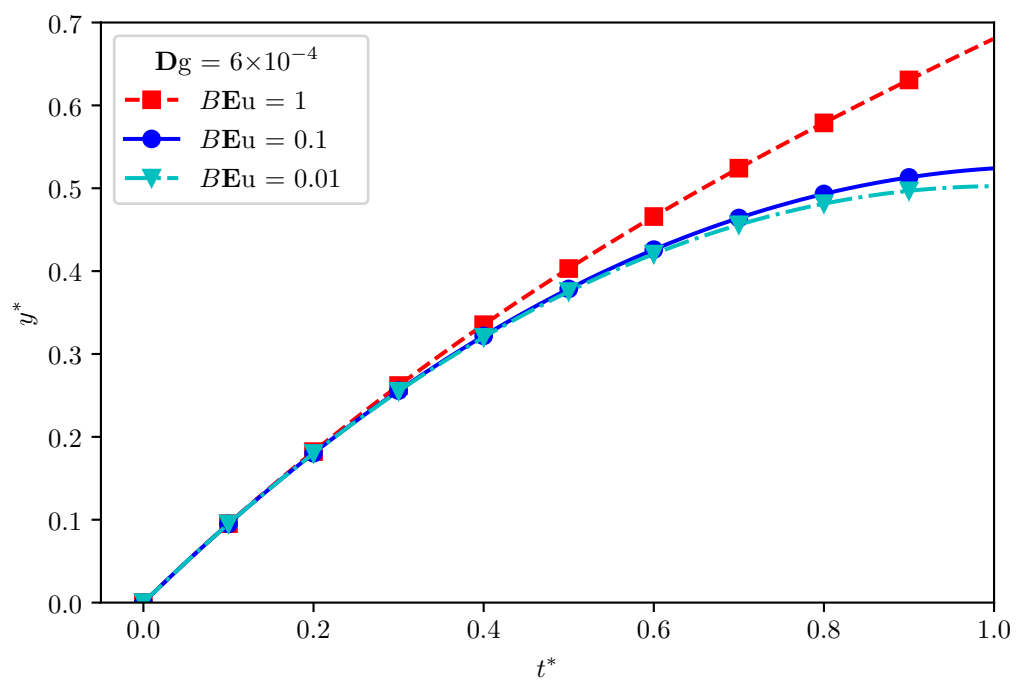


Figure 2.4: Long-time scaled drop trajectories for various values of $B\bar{E}u$.

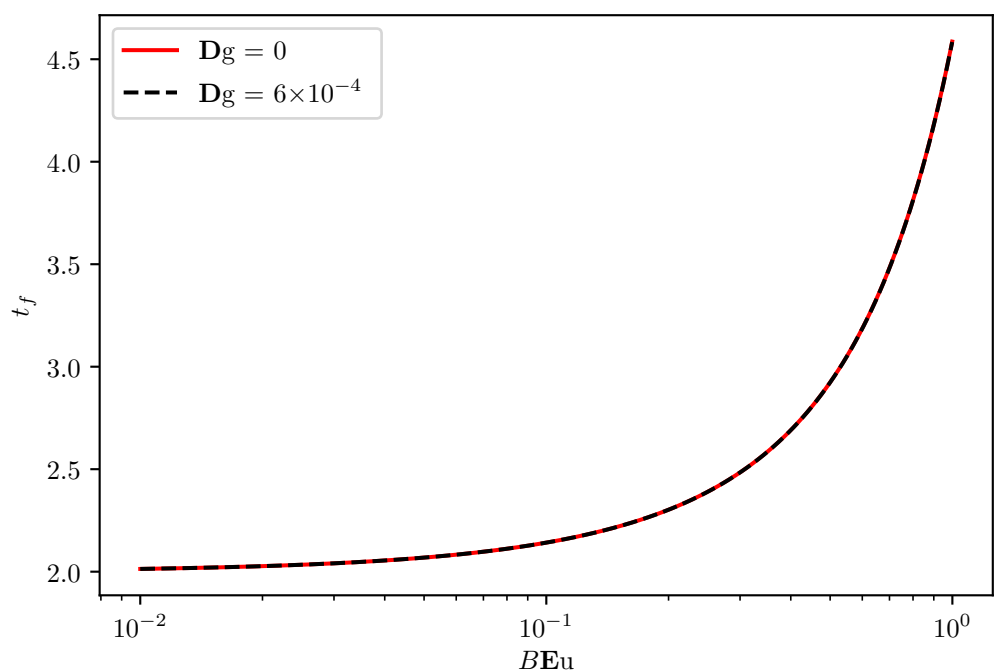


Figure 2.5: $\mathcal{O}(B^3\mathbb{E}u^3)$ accurate asymptotic estimate of drop time-of-flight t_f .

Chapter 3

Methodology

3.1 Overview

We are interested mainly about which parameters are important in electrostatic transport of relatively large millimetric drops in low-gravity, and what the values of the respective dimensionless numbers might be; namely, \mathbb{I}_g , and \mathbb{E}_u . However, this raises an interesting challenge; it is impractical to directly measure all of the key physical quantities that appear in the dimensionless groups at once in a drop tower experiment. In particular, determination of net drop free electric charge q , is difficult as high-input resistance electrometers are not well-suited to sudden the $15-g_0$ decelerations characteristic of drop tower experiments. Schematic representations of drop jump statics and dynamics are shown in Figures 2.2 and 3.1. To find typical values of these parameters we use the following approach:

1. We vary the independent variables V_d , and σ in a set of single-drop spontaneous drop jumps on charged dielectric super-hydrophobic substrates under low-gravity conditions in a 2.1 s drop tower.
2. We capture high-speed video, and digitize the trajectories of the drops.
3. We solve the inverse problem to find the key parameters by maximizing a statistical likelihood function between an observed trajectory and the trajectory predicted by a dynamical model given that certain set parameters.

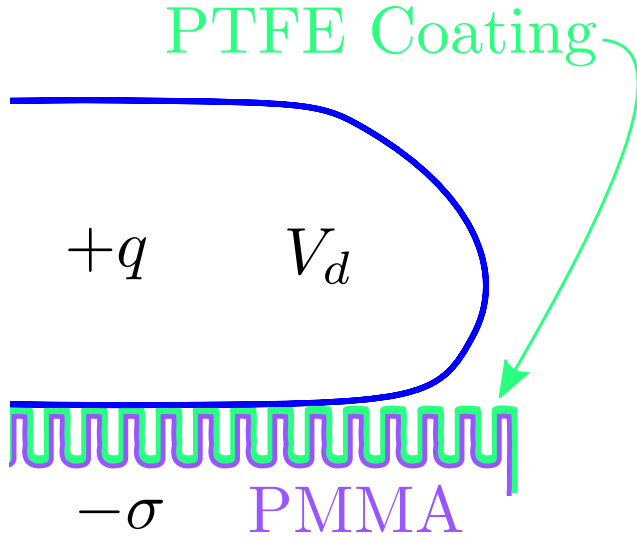


Figure 3.1: A schematic representation of the drop initial condition, resting on the superhydrophobic surface in the Cassie-Baxter state just prior to the drop tower experiment. The variables q , σ , and V_d are the drop net free charge, dielectric surface charge density, and drop volume respectively.

3.2 Experimental Methods

The DDT uses a dual capsule design, inspired by the 2.2 s facility at NASA Glenn Research Center, which decouples drag acceleration felt by the external drag shield from the experiment. The experiment experiences approximately $\lesssim 1 \times 10^{-4} g_0$ during free-fall for the 2.1s as the rig and drag shield plummet to the bottom of drop tower 6 stories below. Single drops of distilled water in a range of volumes ($0.01 \leq R_d \leq 0.5$ mL), are carefully deposited on charged superhydrophobic substrates using a grounded glass syringe with $\pm 1 \mu\text{L}$ accuracy and then dropped in the drop tower. Red dye is added to improve thresholding accuracy in trajectory digitization. Drop trajectories are recorded using a Panasonic HC-WX970 Camera, at 120 fps with 1/3000s shutter speed. In a few cases where higher frame rates are required a Nikon 1 J1 400 fps camera with a 30mm telephoto lens is used. The test cell is back illuminated with a diffused 6000K LED strip light source.

Superhydrophobic electrets are prepared, with surface potentials $\varphi_s = 0.7\text{-}4.0$ kV. According to a review by Sessler [sessler•electrets•1987], an electret is a dielectric material with quasi-permanent electric charge in the sense that the characteristic decay period of the electret is much greater than a practical experiment time scale. Electret charge may be ‘true’ charge in the form of surface or space charges, or polarization charges such as bound

charges. If the electret is not screened by a conductor then it produces an external electric field if the polarization and real charges do not uniformly compensate each other throughout the volume of the electret. For this reason electrets are thought of as electrostatic analogs to permanent magnets. The name *electret* itself is a portmanteau to that effect conjured by Heaviside in 1892[heaviside electrical 2011]. Typical commercial electrets are PTFE films on the order of 10-50 μm thick with the charge being primarily real surface charge. Electrets have a plethora of applications, but most germanely they have been used in Electro-Wetting On Dielectric (EWOD) devices for low-voltage manipulation of small drops[wu low-voltage 2010]. Real charge electrets can be produced by contact electrification, injection or deposition of charge carriers by discharge or electron beam, ionizing radiation, or by frictional triboelectrification. Dipolar electrets by contrast are produced by a combination of polarization at elevated temperatures in a strong external electric field followed by an annealing process. Effective surface charge densities are limited to the material dielectric strengths due to internal dielectric breakdown phenomenon which typically occurs before external breakdown or Paschen breakdown.

We use an isothermal electret formation process using a variation of the widely applied corona-charging technique. Typical corona-charging techniques uses strong inhomogenous DC electric fields to produce discharge in air at ambient conditions; the dielectric substrate is atop a grounded electrode and there is a screening potential electrode intermediately positioned to control the surface potential. The surface potential of the dielectric will tend to saturate at this grid potential if the material is not space-charge current limited. The corona field is usually produced by a pin-shaped electrode. In air the most common charge carriers thus produced are CO_3^- ions. This approach is known to generally produce samples with fairly uniform surface charge densities. Some work[van turnhout thermally 1975] by van Turnhout using Thermally Stimulated Current (TCS) measurements showed that in 4.8 mm thick polymethyl methacrylate (PMMA) polarization of the dielectric is non-uniform due to real space-charge mostly ($\sim 90\%$) residing in a thin (0.1-0.2 mm) layer near the free-surface of the sample. In this work we use a Ptec IN5120 balanced AC corona ion source, to direct a net neutral stream of ions towards the dielectric target, which we polarize by an electrode with a EMCO P20P 2 kV+ absolute reference DC-DC converter. The ion stream compensates the surface and space bound charges arising due to the polarization of the dielectric. When the DC-DC converter is switched to ground the deposited negative ions remain on the surface.

The electret is lamina of 3-4 0.4 mm thick corona charged PMMA sheets. The electric field strength scales with the number of dielectric lamina as has

also been shown in work on electret based vibrational energy harvesters[wada stacking 2012] and in water desalinization[ni desalination 2005].

The electret is established on a superhydrophobic substrate produced by laser etching PMMA and depositing a thin layer of PTFE on the roughened surface. The surface charge density can be modulated during the experiment using the high-voltage DC-DC converter, which can re-polarize the dielectric substrate by means of an embedded electrode, and the resulting bound charge partially or fully neutralizes the electric field due to the surface ions deposited by corona charging of the electret. The high-voltage system is armed manually before the drop tower experiment and is automatically safed by a high-voltage power switching relay, which switches the load across a 100 k Ω resistor when triggered by the resumption of 1-g₀ conditions. The safing is set by an accelerometer pin-interrupt triggered microcontroller command. The rig with a mounted experiment is shown in Figure 3.2.

Contact angles of distilled water on the electret are $\sim 150^\circ$. The hysteresis of the contact angle (the difference between the advancing θ_a and receding θ_r contact angles) is estimated from the roll-off angle using the method of Furmidge[furmidge studies 1962], and is found to be approximately $25^\circ \pm 10^\circ$ when the surface is uncharged. The contact angle for water on smooth PTFE layer is $\approx 115^\circ$ and is further enhanced by an air layer maintained in the underlying roughness length scales of the surface. We use a laser-etched pillar geometry with pillar heights $\sim 775 \mu\text{m}$, widths $\sim 70 \mu\text{m}$, and pitch $\sim 100 \mu\text{m}$. An SEM image of the pillar geometry is shown in Figure 3.4.

Surface potentials φ_s , are measured on the superhydrophobic surface using a Simco-Ion FMX-004 electrostatic fieldmeter and the method for determination of surface charge density for low conductivity polymers described in Davies[davies examination 1967]. This measurement is made with the superhydrophobic surfaces connected by a conductive ground plane by conductive tape far from the presence of other conductors. An ideal approach to determining surface charge on a dielectric surface is to screen perturbing effects of external electric fields. This is partly accomplished by grounding the fieldmeter and by placing the dielectric sample on a grounded conductive plate backing. In this case the surface charge density is determined from

$$\sigma = \frac{\varphi_s \kappa \epsilon_0}{l},$$

where l is the thickness of the dielectric surface. The measured surface voltage is a function of position away from the charged dielectric. In most cases this function is relatively constant at a distance of about 1-2 cm away from the surface though we note that there is some measurement error in surface voltage due to small mispositioning of the electrostatic fieldmeter, say by

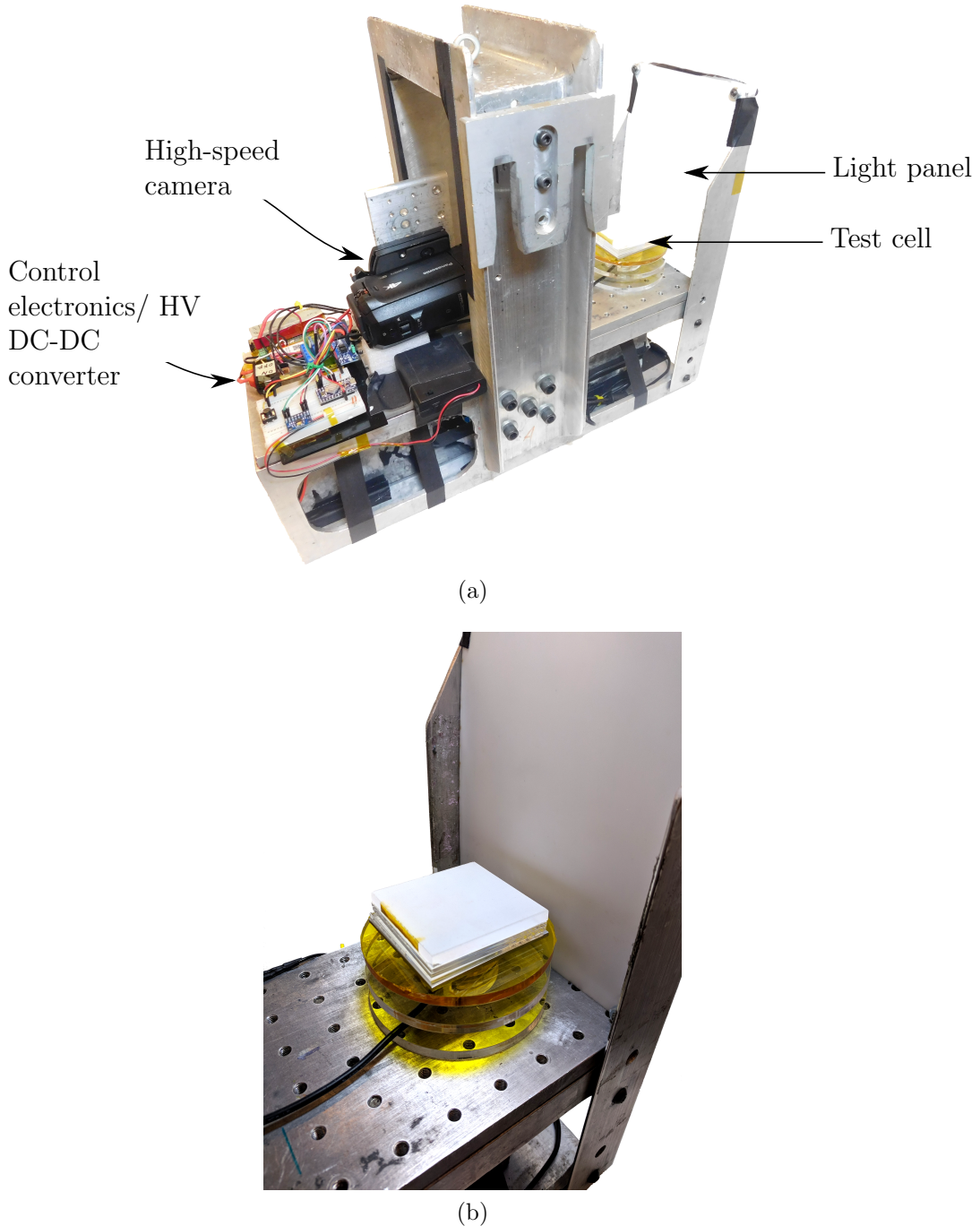


Figure 3.2: (a)The drop electro-bounce experiment hardware mounted on a drop tower rig. (b) Close up of the experimental test cell.

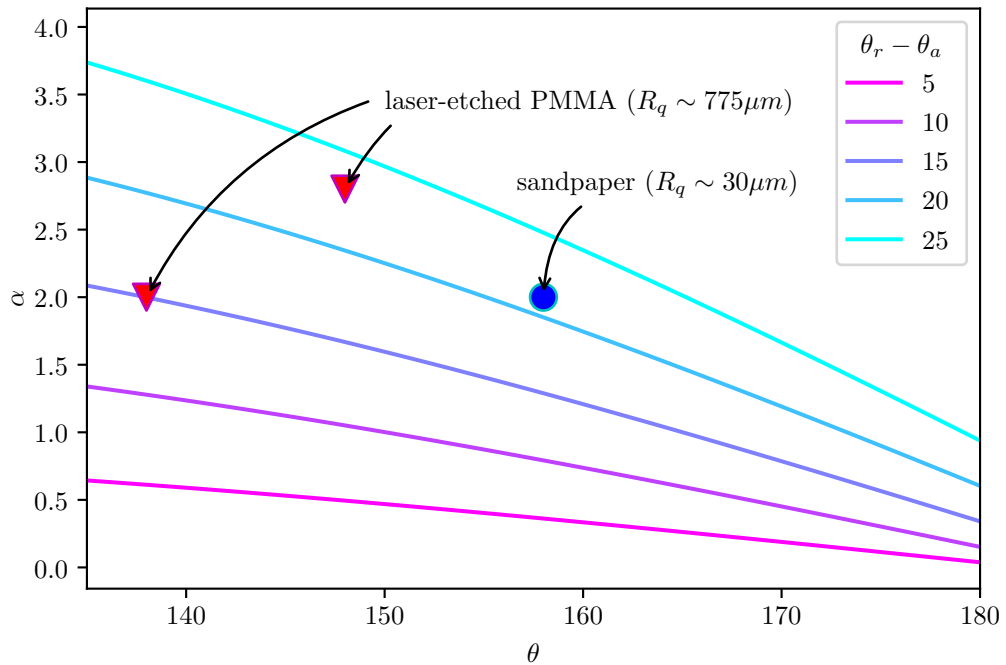


Figure 3.3: The Furmidge model of the hysteresis of the contact line plotted as a function of static contact angle θ , and roll-off angle α , for 1 mL drops. The measured static contact angles, and roll-off angles of several superhydrophobic surfaces including the laser-etched PMMA used in this work are also shown annotated with the characteristic roughness lengthscale R_q of the surface.

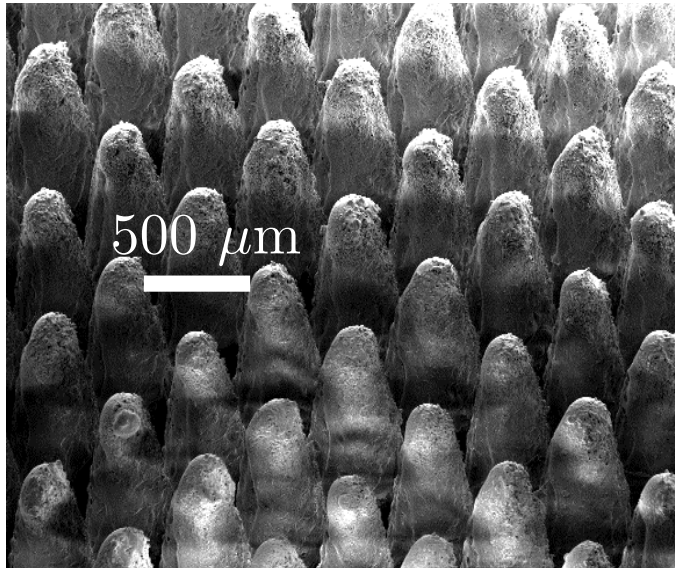


Figure 3.4: SEM image of the superhydrophobic surface.

± 1 mm. The relative dielectric constant of the PMMA sheet is measured by using a 65×65 mm polished aluminum parallel plate capacitor with $C = \kappa\epsilon_0 \frac{A}{t}$ where C is the capacitance, and A is the sheet area. Measuring the capacitance with 3 sample thicknesses using a GenRad 1657 RLC Digibridge, we find the relative permittivity to be $\kappa = 3.5 \pm 0.4$.

A further consideration is the possibility of the change in total charge during a typical experimental timescale. If we consider the drop rig to be a ground which is reasonable given that the rig is isolated from true ground, but is at some reference voltage with respect to the surface charges on the dielectric with an abundance of free charge carriers, then there will be both bulk and surface decay of the charge on the dielectric. The evolution of the charge can in some cases be approximated by

$$\sigma = \sigma_0 e^{\frac{-t}{\kappa\rho}},$$

where σ_0 is the initial surface charge density, and ρ is the bulk resistivity. For an example case of a surface with relative permittivity $\kappa = 3.5$ and bulk resistivity $\rho = 1.6 \times (10^{16}) \Omega\text{cm}$ such as with the case of a 2.8 mm PMMA sheet, then the time constant $\tau = \kappa\epsilon_0\rho$ is approximately 5000 s, which is significantly longer than the typical time period for a drop tower experiment. We measured the charge decay with a calibrated probe at periodic intervals. There are several charge decay mechanisms: internal ones such as Ohmic resistance, and external ones such as compensation by environmental ionic species. The relative magnitudes of these charge transport

mechanisms, and therefore the stability of the electret, vary drastically depending on the initial surface potential, material properties, environment, and charging method. In the case of unshielded electrets compensation by atmospheric ions is significant[perlman·electrets·1973]. Because environmental convection will tend to maintain a gradient of these ions, sealing an electret in a container from the atmosphere will effectively halt this decay mechanism. Atmospheric humidity and water drop condensation can also significantly increase charge decay, presumably by reducing the surface resistance[haenen·characteristic·1975]. Examples of this decay can be seen in Figure 3.5 for differing numbers of dielectric lamina used in this experiment. In looking at the trends in charge decay for our electrets we notice firstly that the decay does not appear to be exponential, as in the model described above. Secondly, we plainly see a cross-over effect in the decay of the surface potential in our electret samples, whereby the samples charged to higher initial surface potentials decay faster and reached the lower overall final potentials. This is a well known effect in polyethylenes charged by corona[ferreira·corona·1992].

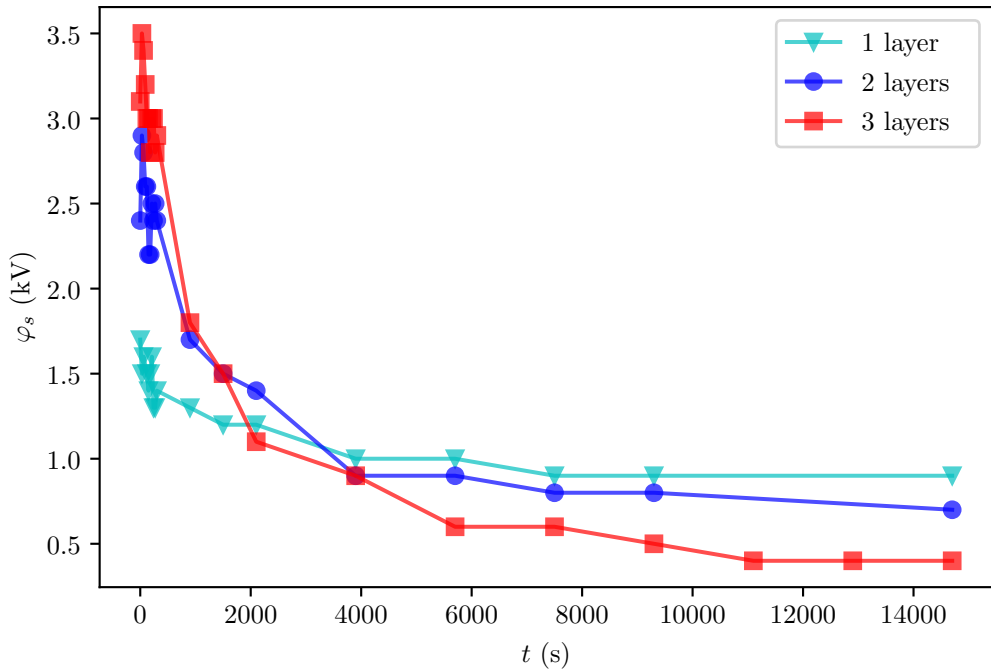


Figure 3.5: Charge decay in the dielectric laminates for several numbers of layers.

3.3 Data Reduction

Digitization of drop trajectories requires several steps of post-processing. Video is first decomposed into a sequence of still images. Trajectories are captured using the particle tracking module in Fiji[[schindelin’fiji:’2012](#)], a derivative of the popular ImageJ[[schneider’nih’2012](#)] package for scientific image analysis. The series is stabilized to remove the effect of drop transients from the kinematic data[[li’image’2008](#)]. The series of still images is cropped and the low-entropy pixels are removed using a built-in rolling ball algorithm. Each still is then split into its constituent RGB maps. In this case the green channel images contain the most information. These are globally thresholded using the Triangle algorithm to recover a map of the pixels corresponding the approximate position of the drop in the original still image. Ellipses are fitted to the pixel map stepping through the time series to determine the positions of the center of mass and the semi-major and semi-minor axes of the drops during the drop tower test. Finally, a perspective correction is applied to the center-of-mass positions.

The code, raw data, and make files for this thesis are archived on the open-source project portal Github[[schmidt’droplet’electro-bounce:’2017](#)].

3.4 Parameter Estimation

Using various scaling arguments we have gleaned from our simple model a series of dimensionless numbers characteristic of drop bounce apoapses and times of flight. These dimensionless numbers depend on physical properties. Unfortunately, not all of these properties are easily measured by experiment. Drop free charge q , in particular, could in principle be directly measured by collecting the charged drops in a faraday cup under low-g and measuring the change in capacitance of the cup using a high input-resistance electrometer, but this method is difficult to apply in practice in a drop tower. Other state variables we can directly measure with varying levels of accuracy.

To measure the charge q we must use parameter estimation techniques. Our work flow to identify q in an individual drop tower experiment is as follows:

1. Experimentally vary V_d and σ , capturing drop trajectories using a high-speed camera.
2. Digitize drop trajectories via automatic tracking of ellipse-fitted centers of mass on the thresholded video.

3. Slice drop trajectories by their bounce minima and apply a smoothing filter.
4. Extract the drop charge, as well as other experimental parameters, by maximizing the log-likelihood of the data given the dynamical model by varying the parameter vector using a direct search optimization.

Mathematically we state that we find the parameters \mathbf{x} that solve the inverse problem $G(\mathbf{x}) = \mathbf{d}$ using the Nelder-Mead direct search method to maximize the log-likelihood of the data. This is equivalent to minimizing the χ^2 goodness-of-fit between an experimentally observed droplet trajectory and the trajectory predicted by Equation 2.7 given a vector of parameters $\mathbf{x} = \langle q, V_d, \sigma \rangle$. This problem is stated as

$$\min \chi^2 = \min \sum_{i=1}^n \frac{(y_d(t)_i - y_G(t, \mathbf{x})_i)^2}{\sigma_{di}},$$

$$\mathbf{x} = \begin{cases} q \\ V_d \\ \sigma \end{cases} \text{ subject to constraints } g = \begin{cases} V_d \pm u_{exp} \\ \sigma \pm u_{exp} \\ y_0 \pm u_{exp} \\ t_0 \pm u_{exp} \end{cases}$$

where $y_G(t, \mathbf{x})$ is the y -coordinate position at time t of the numerical solution of the equation of motion

$$my'' = \frac{1}{2}\rho C_D A_d y'^2 + qE(y) + Kq^2 y^{-2},$$

$y_d(t)$ is the corresponding experimentally observed drop y -coordinate position at time t , and σ_d is the standard error of the observed position. The vector \mathbf{x} that minimizes χ^2 is the so called Maximum Likelihood Estimate (MLE) of the experimental parameters. This approach is given further explanation below.

3.4.1 Inverse Problems

Suppose we have a model $G(\mathbf{x})$ with a vector of parameters \mathbf{x} and set of ideal observations \mathbf{d} . We then expect there to exist a relationship

$$G(\mathbf{x}) = \mathbf{d},$$

where the operator G might be an ODE. Suppose the model $G(\mathbf{x})$ is the ODE

$$y'(t) = f(t, \mathbf{y}; \mathbf{x}), \quad \mathbf{y} \in \mathbb{R}^n,$$

and a collection of n measurements of experimental data

$$\mathbf{d} = (t_1, \mathbf{y}_1), (t_2, \mathbf{y}_2), \dots, (t_k, \mathbf{y}_k).$$

The process of fitting a function defined by a collection of parameters to a data set is called the discrete inverse, or parameter estimation problem as opposed to the *forward problem* to find \mathbf{d} given \mathbf{x} and $G(\mathbf{x})$. This is a familiar procedure when the determination of model parameters is accomplished using linear or polynomial regression. However there are approaches even to fitting an arbitrary function to a noisy and sparse dataset. In this work we use the conventional Maximum Likelihood Estimate method to identify the model parameters.

Using MLE we seek to know what is the probability that this data set occurred given the set of model parameters. In other words, what is the likelihood of the parameters given the data. Bayes' Theorem holds that

$$\text{prob}(X|D, I) = \frac{\text{prob}(D|X, I) \times \text{prob}(X|I)}{\text{prob}(D|I)}$$

where D are the observations (dataset), X is the vector of parameters, I is general background information about the problem including the mathematical model, and

$\text{prob}(X D, I)$	posterior probability density function,
$\text{prob}(D X, I)$	likelihood function,
$\text{prob}(X I)$	prior probability density function,
$\text{prob}(D I)$	evidence.

The posterior probability density function (PDF) $\text{prob}(X|D, I)$ is ultimately what we wish to estimate, the prior PDF $\text{prob}(X|I)$ reflects our knowledge of the system, and the evidence $\text{prob}(D|I)$ is the likelihood of the data based on our knowledge. We also note that since it only makes sense to compare the conditional PDF's for the same data, we can ignore the denominator. We further note that the prior $\text{prob}(X|I)$ is fixed before our observations and so can be treated as invariant to our problem. We can therefore infer that $\text{prob}(X|D, I) \propto \text{prob}(D|X, I)$. The MLE for the model parameters \mathbf{x}_0 is given by the maximum of the posterior PDF, which is equivalent to the solution of the ODE given the the parameters \mathbf{x} , that produces the highest probability of the observed data. Since the likelihood $\mathcal{L}(\mathbf{x}) = \prod_i^n \mathcal{P}_i$ and the probability \mathcal{P} of any single observation is less than one, then the total likelihood which is the product of a large number of probabilities is vanishingly small. The more well-behaved log-likelihood is given by

$$\mathcal{M} = \ln(\mathcal{L}) = \ln(\text{prob}(D|X, I)) = \text{const} - \frac{\chi^2}{2},$$

where

$$\chi^2 = \sum_{i=1}^n \frac{(y_{di} - y_{Gi})^2}{\sigma_{di}^2}$$

is the χ^2 goodness-of-fit, $y_d = y_d(t)$ is a observation of drop position at a point in time, and $y_G = y_G(t, \mathbf{x})$ is the drop position predicted by the solution to the equation of motion at time t , and σ_d is the standard error of the position measurement. The optimal parameter set is the one with the highest probability of observing the data (the maximum of the posterior PDF) and can be determined by maximizing the log-likelihood \mathcal{M} (or minimizing χ^2) of the data \mathbf{d} with respect to the parameter set \mathbf{x} . Thus parameter estimation is a variety of optimization problem.

3.4.2 Smoothing

All optimization methods, whether explicitly or implicitly, follow gradients towards an optimum. In a parameter estimation problem, if we approximate these gradients by finite differences, then the noise manifests itself as amplification of the roughness in the hyper-response surface. Gradient-based optimizers do poorly in these situations because they tend to converge to local minima. While so called gradient free algorithms offer an improvement in this regard, speed of convergence and the quality of the MLE is improved by smoothing the objective function. This is equivalent to smoothing the underlying dataset.

Our choice of smoothing approach depends principally on the nature of the errors in the dataset. The sources of error include misalignment of the camera, error in the fiduciary length scale, perspective due to objects being out of the photographic plane, and various errors arising in the digitization process including the difference between the thresholded ellipse fitted centroid and the true centroid of the non-ellipse drop centroid. Some of these errors are systematic in origin and introduce consistent biases into the data, e.g., coherent spectral sources, rather than truly stochastic noise. Data smoothing does little to help systematic errors in that they are usually of lower frequency than the signal. Random errors, by contrast, are assumed to have a Gaussian distribution as required by the central limit theorem, and are independent of the signal which we assume results from an inherently deterministic process.

We experimented with a variety of filters implemented in the `scipy.signal` Python *SciPy*[[oliphant·python·2007](#)] module on a representative set of trajectory data; these methods include 1D Gaussian convolution, Wiener, Butterworth, and Savitsky-Golay filters. Qualitatively comparing these smoothing methods by hand tuning filter orders and window sizes, we find that

we loose too many data points in the smoothing process, large amplitudes are overly smoothed by repeated filtering passes, or there are significant end effects for most of these methods. A comparison of these smoothing approaches on a representative trajectory data set is shown in Figure 3.6.

The Savitsky-Golay, and Butterworth filters both produce fairly smooth derivatives as can be seen in Figure 3.6, but the small window-size needed for Butterworth filter tends to also produce a noticeable end effect. The Savitsky-Golay filter essentially uses a moving-window based on local least-squares polynomial approximations. It was shown that fitting a polynomial to a set of input samples and then evaluating the resulting polynomial at a single point within the approximation interval is equivalent to discrete convolution with a fixed impulse response[savitzky'smoothing'1964]. A beneficial property of this kind of low-pass filter is the tendency to maintain waveform amplitudes, and so they are attractive in applications having noisy signals with sharply pointed waveforms such as ultrasound or synthetic aperture radar[schafer'what'2011]. Because Savitsky-Golay is a Finite Impulse Response (FIR) filter it requires data points to be equally spaced. To accommodate this requirement we interpolate points between the small gaps which sometime occur in the tracking results from image analysis. We use a moving window size slightly smaller than the length of the current bounce in a single drop jump data set. The windows are piecewise defined by partitioning the data set into a series of individual bounces. To this partitioning is accomplished by slicing the dataset at minima identified after an initial rough smoothing pass using the `scipy.signal.argrelextrema()` function. The Savitsky-Golay polynomial order is 4.

To understand how these filters differ it is useful to look at their frequency responses. The power spectra for these same data, obtained by Discrete Fourier Transform, are shown in Figure 3.7. Though, it is worth noting that our signal is not truly periodic.

3.4.3 Optimization

Most generally, a constrained optimization problem is stated as

$$\begin{aligned} \text{minimize: } & f(\mathbf{x}) && \text{objective function,} \\ \text{subject to: } & g_j(\mathbf{x}) \leq 0 && \text{inequality constraints,} \\ & h_k(\mathbf{x}) = 0 && \text{equality constraints,} \end{aligned}$$

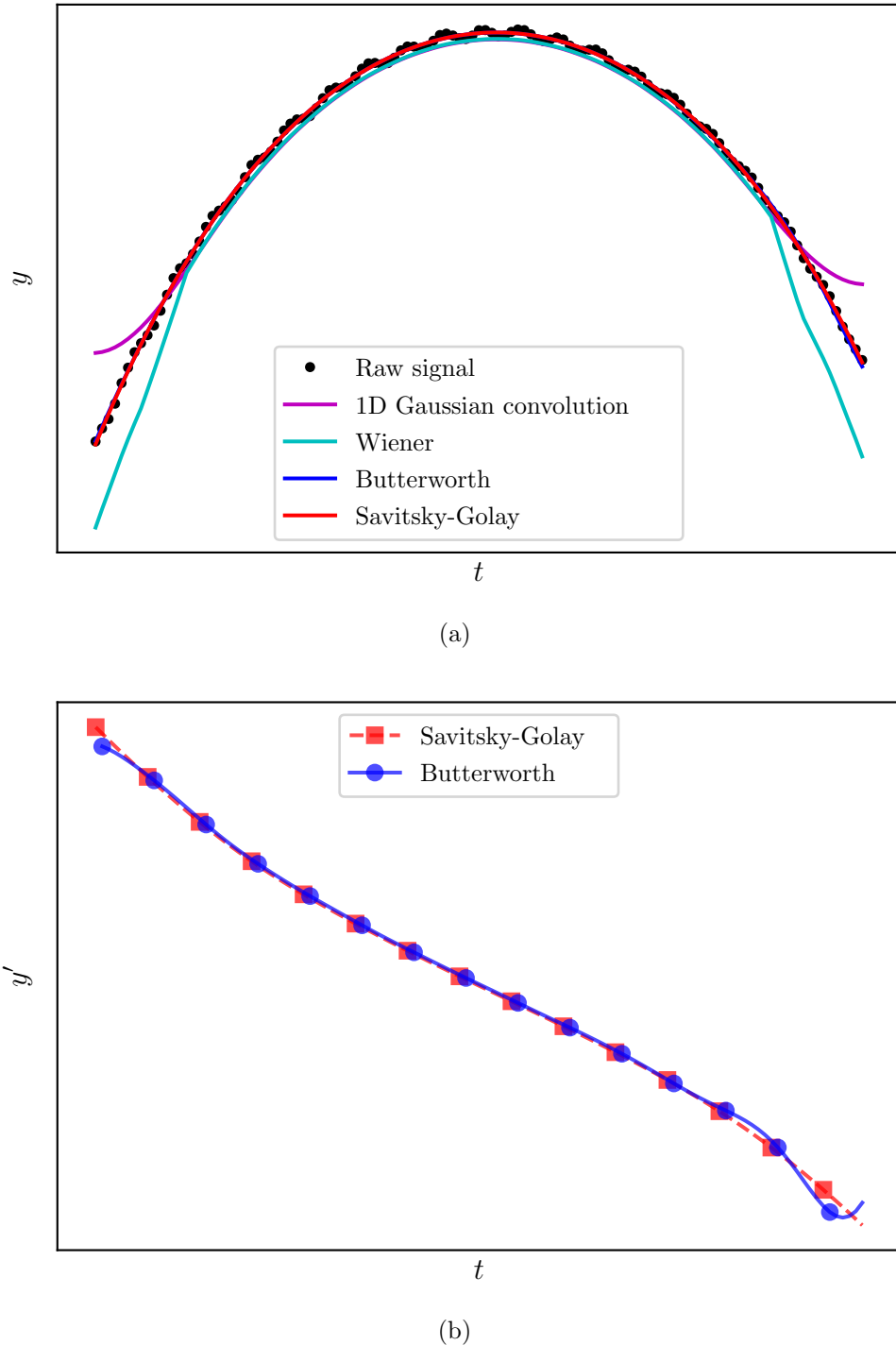


Figure 3.6: (a) Schematic noisy droplet trajectory data. We see that 1D Gaussian convolution and Wiener filters suffer from significant end effects. At this scale Butterworth and Savitsky-Golay filters are nearly indistinguishable. (b) Comparing Butterworth and Savitsky-Golay filtered first derivatives of the above schematic trajectory we see that the Butterworth filter also suffers from a slight end effect. This implies that the optimization will find a different optima of the likelihood depending on which type of filter is used.

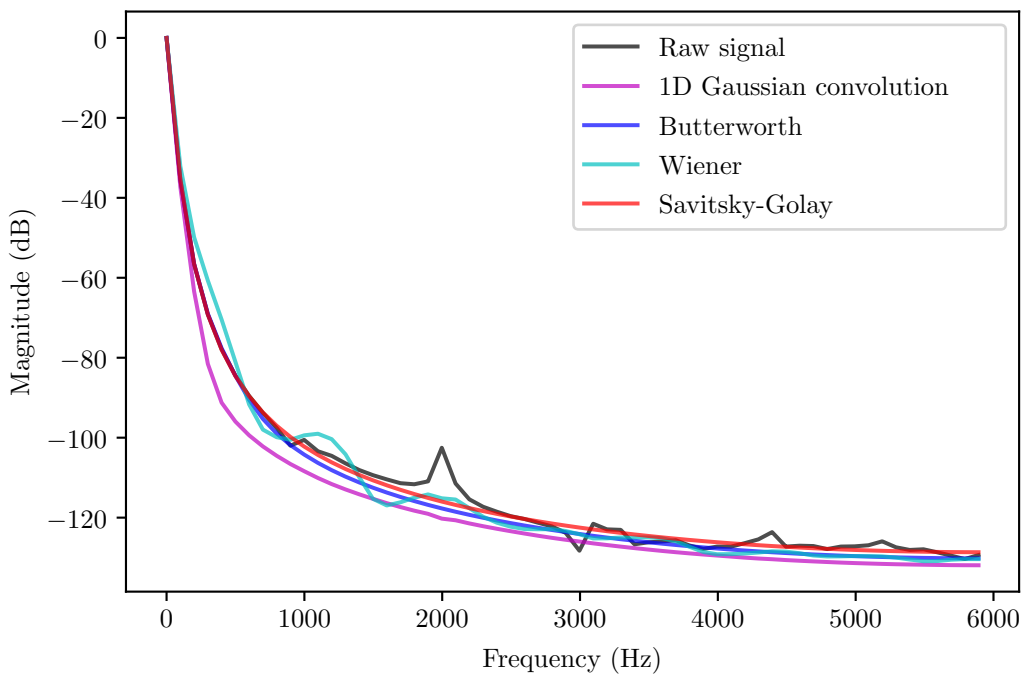


Figure 3.7: The power spectra has a peak at 1 Hz, which is the drop trajectory parabola itself, and smaller peaks in the kHz range corresponding to various noise frequencies. The Savitsky-Golay and Butterworth filters seem to have the least distortion of the power spectra of the true signal. Both also attenuate the noise at the 2 kHz peak.

$$\text{where } \mathbf{x} = \begin{pmatrix} x_1 \\ x_2 \\ \vdots \\ x_n \end{pmatrix} \quad \text{design variables.}$$

Mathematical optimization is the problem of finding minima of a function f . In this context the function is called the cost, or objective function. The field of mathematical optimization is as old as calculus itself, and the number of particular optimization techniques is correspondingly myriad. Particular techniques lend themselves well to particular types of optimization problems. The minima of the objective function f is sought on a domain A specified by the constraints of the problem, where the domain is usually called the feasible region. Minima of objective function $f : A \rightarrow \mathbb{R}^m$ are called feasible solutions. If the function f is convex the feasible solution is the global minimum, otherwise additional local minima exist. The scale of the optimization problem is set ultimately by dimensionality of the objective function. Functions may not always be smooth in the sense of having continuous derivatives, and this is problematic in that optimization methods fundamentally rely on gradients of the objective function. Problems with anisotropic objective functions where there is strong covariance between the parameters, and the gradient vector generally to differ significantly from the Newton direction $-\mathbf{H}^{-1}f'(\mathbf{x})^T$, where \mathbf{H} is the Hessian matrix, are considered ill-conditioned. Gradient based deterministic search algorithms tend to converge slowly for ill-conditioned problems as they take a zigzagging path determined by the local value of the gradient rather than following the Newton-direction vector towards the minimum. Numerical optimization may deal with black box functions where we do not have an explicit mathematical expression of the function we are optimizing. Black box problems are challenging because we do not have access to analytic gradients of the objective function and approximating them by finite-differences is slow and noisy. In general, noisy, black box, non-linear, non-quadratic, non-convex, constrained, ill-conditioned, high-dimensional objective functions are problematic to optimize. Unfortunately, problems of this type are the essence of the parameter estimation, which often leads to its characterization as an ‘art’ rather than a precise science.

The equation of motion behaves stiffly due to the large disparity in Coulombic and image charge length scales. We integrate it numerically using the `odeint` *Scipy* module. This is a shake-and-bake Python wrapper for the venerable 1982 *netlib ODEPACK* library double-precision `lsoda` integrator [**hindmarsh·odepack·1983**] (Livermore Solver for Ordinary Differential equations with Automatic method switching for stiff and nonstiff

problems). The function switches dynamically between Adams (nonstiff) and Backwards Differentiation Formulas (BDF, stiff) according to the stiffness of the solution.

Our specific optimization problem is non-convex, mixed discrete-continuous black-box (noisy), and highly ill-conditioned which is essentially the worst case scenario for an optimization problem. The ill-conditioning arises due to the strong covariance between several of the model parameters, particularly $q = q(V_d, E_0)$. The non-convexity of the problem implies that there are many local minima of the objective function. While in principle a gradient-based optimizer, such as the quasi-Newton method of Broyden, Fletcher, Goldfarb, and Shanno (BFGS)[**nocedal**·numerical·2006], could be used by using finite-differences to obtain approximate gradients of the χ^2 objective function, in practice doing so is extremely problematic because the noise-to-signal ratio of the objective function scales like $\mathcal{O}(f)$ for df/dt and $\mathcal{O}(f^2)$ for d^2f/dt^2 which will tend to cause convergence to a local minima that is only an artifact of the likelihood response surface[**wood**·data·1982]. As a further practical matter, given the relatively expensive function-calls gradient-free approaches tend to offer better performance regardless[**kolda**·optimization·2003], especially when evaluating the objective function requires solving a stiff, non-linear ODE.

We use a gradient-free, direct-search approach: Nelder-Mead[**nelder**·simplex·1965] implemented in `scipy.optimize`. Nelder-Mead is relatively robust to noise and is thrifty with our computationally expensive function-calls. Nelder-Mead, sometimes called simplex-search or downhill-simplex, is a heuristic search method with no guarantee of optimal solutions. It nonetheless is a well-established and widely used algorithm. Nelder-Mead is based on the concept of an N -simplex, which generalizes a triangle into higher dimensions as a polytrope of $N + 1$ vertices in N dimensions. It uses only-function calls and expands or contracts the simplex according to the function values at its vertices in a way visually reminiscent (in \mathbb{R}^3) of the oscillations of the jumping drops themselves. In fact Nelder-Mead is sometimes also called the ‘amoeba method’. Very little is known about the convergence properties of the Nelder-Mead algorithm in its classical form for non-smooth objective functions[**price**·convergent·2002], except that in general it doesn’t satisfy the properties required for convergence by other direct search algorithms: the simplex remains uniformly non-degenerate and some form of sufficient descent condition for function values at the vertices is required at each iteration. Scaling can help solve convergence problems and improve numerical stability. We precondition the optimization problem by minimizing $\ln(\chi^2)$ and using a naive $\sim \mathcal{O}(1)$ scaling of our constraints by their initial guesses. Here the goal is to make the problem equally sensitive to steps in any direc-

tion. Nelder-Mead is not a global optimizer, though there are variants which use sequential local searches with probabilistic restarts to achieve globality, usually at a tremendous computational cost. However, Nelder-Mead behaves less locally than many gradient-based approaches. The convergence history of the parameter MLE using Nelder-Mead for a single drop jump experiment is shown in Figure 3.8. Results of the parameter estimation are shown in Figures 3.9, 3.10.

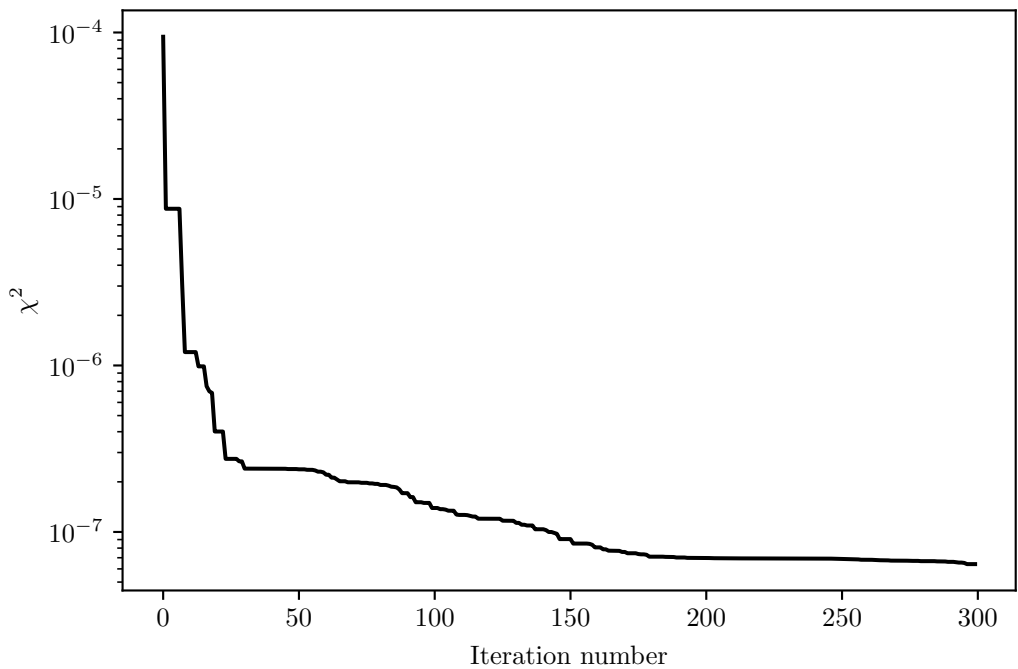


Figure 3.8: As is typical with Nelder-Mead much of the improvement in χ^2 is realized in the first few iterations. Overall the rate of convergence is sub-linear, which is to be expected for non-linear constrained problems using an heuristic algorithm.

3.4.4 Identifiability

That we are capable of fitting any arbitrary model to a dataset given sufficient degrees of freedom in our parameters is admittedly a disconcerting issue, begging the question ‘given the structure of the model is it possible to uniquely estimate the unknown parameters?’ This question is called the problem of identifiability. However, some of the inverse model parameters

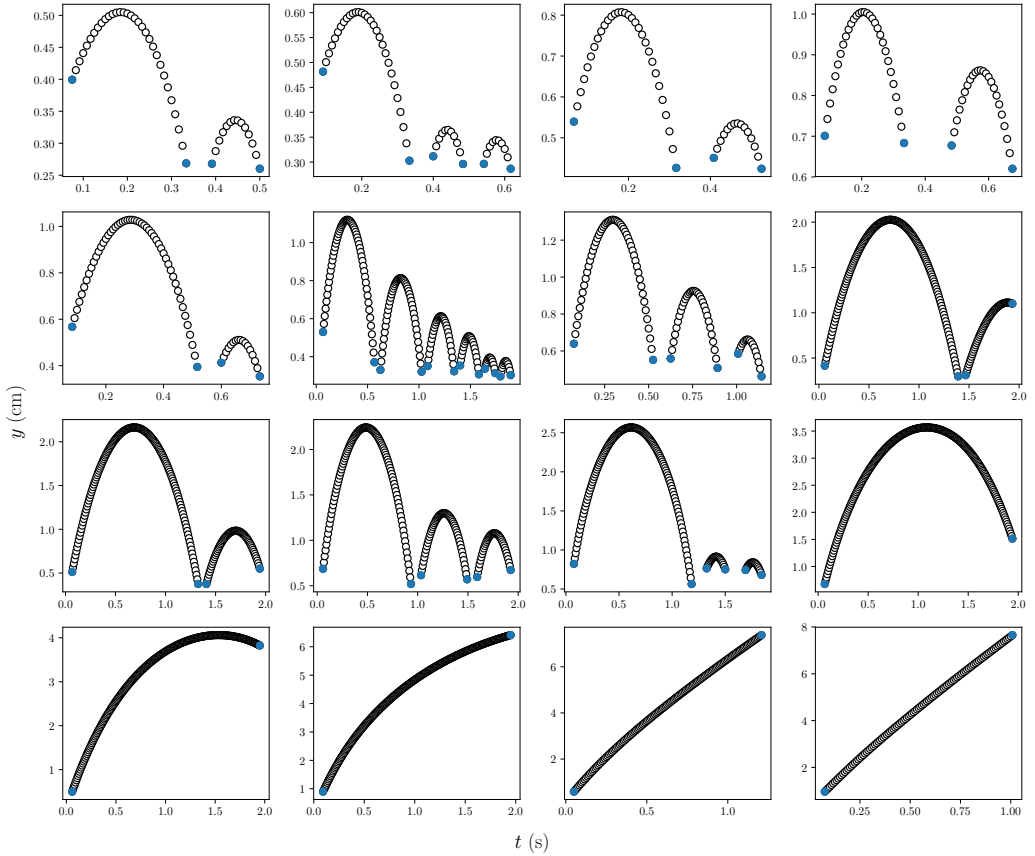


Figure 3.9: A series of filtered drop trajectories arranged by increasing apoapse. The blue dots represent either the beginning and end of the experiment, or points at which the drop is either coming into, or leaving contact with the surface.

are constrained by our experimental observations of them and their associated measurement uncertainties. This, we hope, makes the specter of an over fit model less frightening, but does convert our unconstrained optimization problem to an constrained one which raises special difficulties of its own, which we discuss below.

The Nelder-Mead direct search method cannot be used with explicitly constrained problems. However, there are various implicit approaches to approximately solve general constrained problems using unconstrained algorithms. Generally, this is achieved by domain transformations or the use of penalty functions. By the addition of a penalty function which depends in some way on the values of the constraints to the objective function, we minimize a pseudo-objective function where the in-feasibility of the constraints

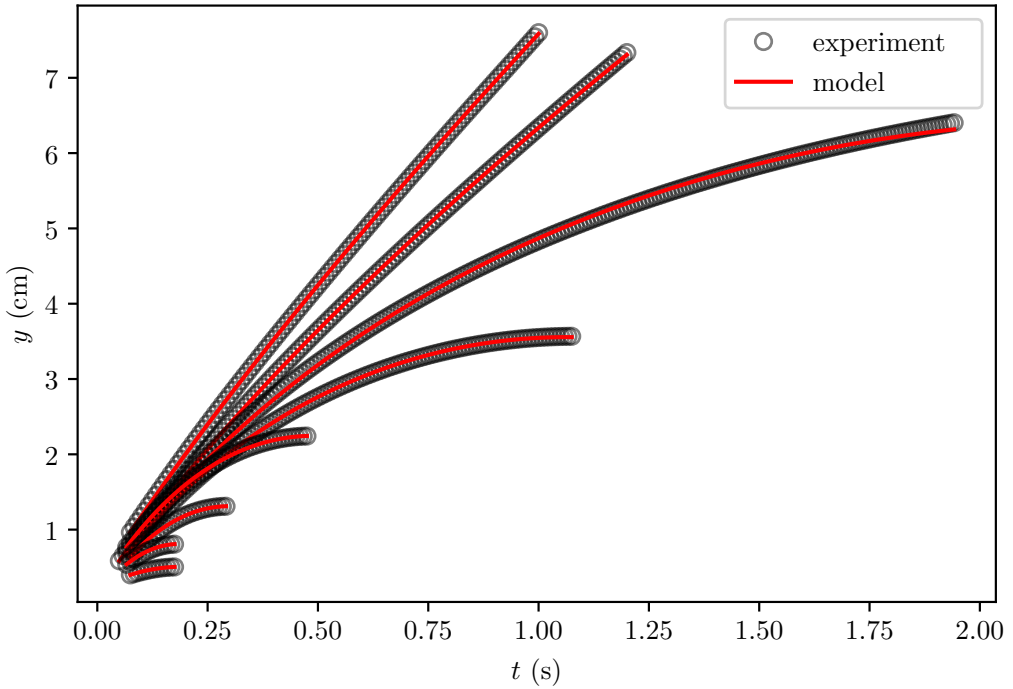


Figure 3.10: A series of drop trajectories showing the results of the parameter estimation. The trajectories are shown only up to the apoapse of the first bounce. The (—) lines show the ODE solution with given the MLE parameter vector. χ^2 goodness-of-fit varies between 1×10^{-5} and 1×10^{-8} with the better fit occurring typically for the drops with the lowest apoapses.

is minimized simultaneously to the objective function.

There are various penalty function schemes. We use an exterior penalty function as a simple way of converting the constrained problem into an unconstrained one. These are especially useful in cases where the constraints are not ‘hard’ in the sense that they need to be satisfied precisely. General penalty functions, which are sequential unconstrained minimization techniques, reformulate the general constrained problem as the pseudo-objective function given by

$$\phi(\mathbf{x}, r_p) = F(\mathbf{x}) + r_p P(\mathbf{x}),$$

where $P(\mathbf{x})$ the penalty function is given by

$$P(\mathbf{x}) = \sum_{j=1}^m \{\max[0, g_j(\mathbf{x})]\}^2 + \sum_{k=1}^l [h_k(\mathbf{x})]^2. \quad (3.1)$$

We see from Equation 3.1 that there is no penalty if the constraints $g_j(\mathbf{x})$ and $h_k(\mathbf{x})$ are satisfied.

As with penalty function approaches generally, the exterior penalty function has several drawbacks; namely, the possibility of the objective function being undefined outside of the set of feasible solutions. Additionally, by naively encouraging feasibility of the solution using large values of the penalty parameter r_p we will tend to ill-condition the unconstrained formulation of the problem, though in our implementation the preconditioning tends to make the pseudo-objective function less and less sensitive to the constraints as the likelihood is approaches a maximum. We use the measured values of u_0 , V_d , and E_0 , and the informed guess $q \approx kV_d^{2/3}E_0$ where k is a constant $k \approx 1^{-11}$ as an initial guess for the parameter vector \mathbf{x} . We stop the optimization after 300 iterations rather than waiting for convergence.

We are interested in the variance and co-variance as a means to determine the quality of the parameter estimate. The (i, j) -th element of the matrix $\sigma(\mathbf{x}, \mathbf{y})$ is equal to the covariance $\text{cov}(X_i, Y_j)$ between the i -th scalar component of \mathbf{x} and the j -th scalar component of \mathbf{y} . Here the concept of error bars in linear correlation associated with a covariance matrix is not suitable. We might try to generalize the idea of confidence intervals to a multidimensional space, but it is difficult to describe the hyper-volume containing a certain percentage of the probability with only a few numbers. The situation is worse if the PDF has several maxima. However, there is another approach to find the covariance matrix, given by

$$[\sigma^2]_{ij} = -\left[(\nabla^2 \mathcal{L})^{-1}\right]_{ij} = 2\left[\nabla^2 (\chi^2)\right]_{ij}^{-1} = -[H^{-1}]_{ij},$$

where H refers to the Hessian matrix and $[\sigma^2]_{ij}$ is the covariance matrix C . The issue of identifiability is especially fraught for non-linear black-box type problems were it is difficult to explicitly evaluate the Hessian. The likelihood function, and thus the posterior probability density function, are defined completely by the optimal solution \mathbf{x} and the second derivative of \mathcal{L} at the maximum, which corresponds to the covariance matrix C . The standard errors, or marginal variances, are the square roots of the diagonal of the covariance matrix. The Hessian matrix must be negative definite for \mathcal{L} to have a maximum at \mathbf{x}_0 . We obtain an approximate Hessian using the approach suggested in Nelder's original paper by fitting quadratics to the simplex vertices and midpoints [nelder·simplex·1965][spendley·sequential·1962]. We use the condition number

$$\text{cond}(H) = \frac{\max[\text{eig}(H)]}{\min[\text{eig}(H)]}$$

to make a qualitative assesment of the stability of the problem. We find typ-

ical condition numbers $\sim \mathcal{O}(10^{27})$. In fact, in many cases our Hessian is not negative definite, or invertible at the minima \mathbf{x}_0 , which implies negative values of the variances, which are impossible. These issues indicate the problem is extremely ill-conditioned near the minima \mathbf{x}_0 . Given that the parameter estimates are highly co-linear, it is unsurprising that the Hessian matrix is near-singular and its inversion is either impossible or involves significant numerical error. Posteriori verification of the results is crucial to bound the identifiability of the parameter estimation problem, but this remains as future work. Several sources suggest sensitivity analysis of the parameter estimates by generation of synthetic Monte Carlo data sets as a means of establishing identifiability[bevington·data·1969][jaqaman·linking·2006].

3.5 Summary

The objectives of our experimental work are to validate the earlier scaling results by identifying values of the physical parameters which appear in the relevant dimensionless groups. To accomplish this we conduct a series of low-gravity experiments in a 2.1 s drop tower, where we observe the trajectories of spontaneous drop jumps and rebounds from charged dielectric superhydrophobic substrates.

- In drop tower experiments we vary the independent variables V_d and σ and capture the trajectories of the droplets using high-speed video.
- We produce superhydrophobic electret substrates with surface potentials 0.7-4.0 kV and contact angles $\sim 150^\circ$ with approximately 25° contact angle hysteresis when uncharged. The dielectrics are a lamina of 3-4 corona charged 0.4 mm PMMA sheets. The electric field scales with the number of dielectric lamina. The superhydrophobic layer of the electret lamina is manufactured by laser etching a $\sim 775 \mu\text{m}$ deep square array of pillars into the PMMA sheet, followed by a PTFE spray deposition process.
- We solve the inverse problem to identify key parameters which we cannot measure directly in the drop tower experiments. This is accomplished by Maximum Likelihood Estimation using constrained direct search optimization.
- We fail to establish the identifiability of the parameter estimate using the conventional approach of inverting the Hessian near the optima. This indicates ill-conditioning of the parameter estimation problem,

likely due to large multicollinearity between the main factors q , V_d and σ . To robustly estimate the error of the parameter estimates an alternate approach, such as the Monte Carlo method, is required.

Chapter 4

Results

4.1 Parameter Estimates

We found the distribution of mostly likely experimental net charges for a population of the drops jumped in low-gravity. A covariance plot of the model variables is shown in Figure 4.1. The multicollinear dependence of charge on drop surface area, A , and the characteristic electric field, E_0 , is evident. Assuming the main effect is the interaction between charge and electric field, a Robust Least Squares model fit $q \sim kAE_0$ (using the Python `statsmodels.formula.api.RLM` function), with the non-linear transformation $A = V_d^{2/3}$, found that $k = 5.01 \times 10^{-11} \pm 2.85 \times 10^{-11}$ with $R^2 = 0.946$. This model uses Huber's T norm, median absolute scaling, and H1 covariance estimation. A contour plot showing the estimated drop free charge as a function of V_d and φ_s is shown in Figure 4.2.

A two-ways T-test comparison of charge distributions between the drop bounce experiment and a corollary experiment with zero electric field at the time of drop deposition on the superhydrophobic surface suggests that the drop charge is induced by the electric field, rather than through contact charging on the PTFE layer ($t = 5.11, p = 0.0002$). The T-test informs us that the charge distribution are about 5 times more different from each other as they are within each other, and there is a 0.02% probability that this result happened by chance. This corollary experiment is documented in Appendix A.

The model $q \sim kAE_0$ is incidentally very similar to the classical solution for the surface charge density of a half-spherical conductor with a

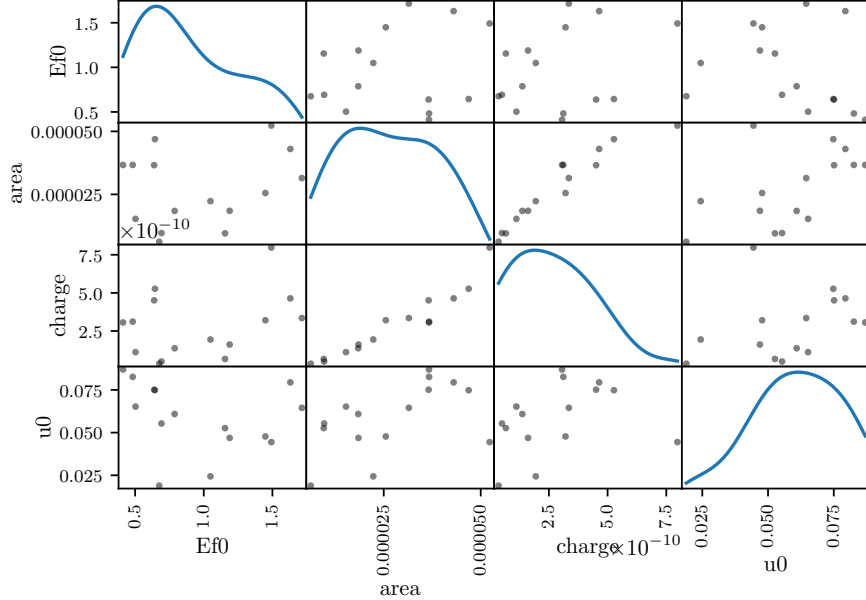


Figure 4.1: Covariance plot of main parameters E_0 , U_0 , droplet area ($V_d^{2/3}$), and q .

field-induced dipole[david j. griffiths introduction 1999]

$$\begin{aligned}
 q &= 3\epsilon_0 E_0 \int_A \cos \theta dA \\
 &= 3\pi^{1/3} 6 (6V_d)^{2/3} \epsilon_0 E_0 \int_{\pi/2}^{4\pi/2} \cos \theta d\theta \\
 &= k E_0 V_d^{2/3}
 \end{aligned}$$

with $k \approx 1.3 \times 10^{-10}$. This is also of a similar form to the charge found by Takamatsu and coauthors for drops falling from a grounded nozzle in an external electric field[takamatsu theoretical 1981]

$$q = 4\pi\epsilon_0\beta E_0 R_d^2$$

with $\beta \approx 2.63$.

4.2 Scale Quantities

The dielectrophoretic force plays a very small role when drops have net charge in a DC field; the condition to neglect the DEP force was satisfied for all

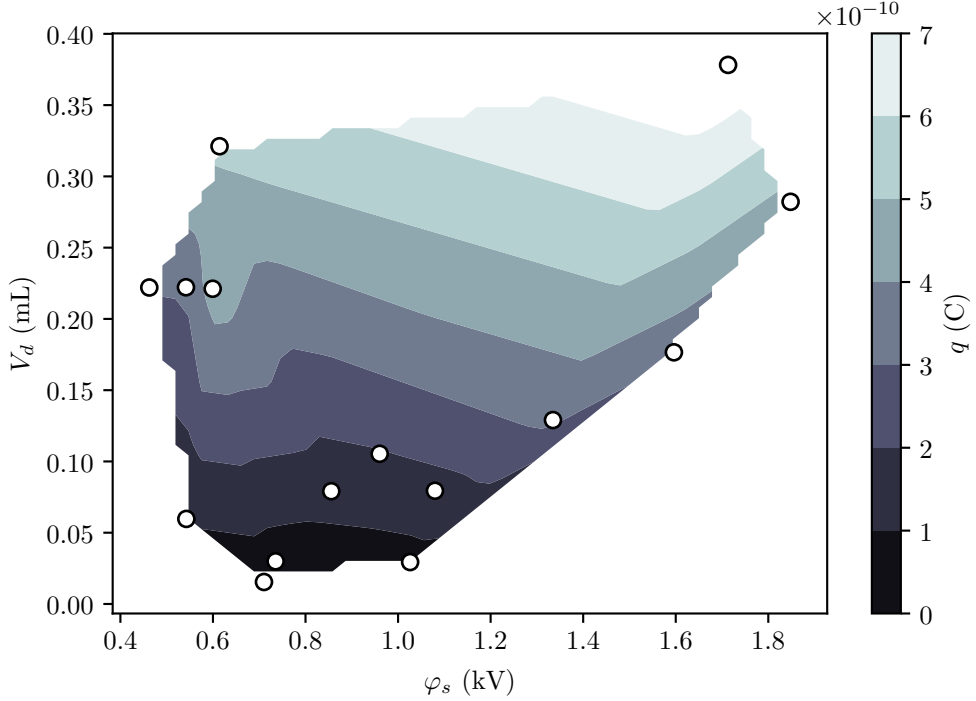


Figure 4.2: Charge q , as a function of V_d , φ_s .

experiments in the dataset. Dimensional drop apoapses scale closely with Eu as seen in Figure 4.3. The relative magnitudes of the simulated forces felt by the drops is shown in Figure 4.4. Forces acting on the drops vary in magnitude between $\mathcal{O}(10^{-6})$ - $\mathcal{O}(10^{-4})$ N. We see that, of the drops in the experimental dataset only the two with the largest Eu , $\text{Eu} \sim \mathcal{O}(1)$ could appropriately be said to be in the inertial electro-viscous regime. In all other cases image forces are much stronger than drag. For these drops $\text{Eu} \gg 1/8\pi$, and are likely on escape trajectories. The image forces themselves rapidly become small compared to Coulomb forces for drops with apoapses $\max(y) \gtrsim L$, thus it is reasonable to claim that for intermediate drops Coulomb force scales as inertia, and we can neglect the effects of drag and image forces.

In the non-dimensional trajectories with short-time scaling shown in Figure 4.6, we see that the trajectory apoapses are consistently $\mathcal{O}(1)$, but most trajectories overshoot their characteristic time scale (which predicts returns at $\bar{t} = 2$ to the first order). We also observe that that Eu is not typically a small number in this regime, imperiling our use of asymptotic estimates in this regime. We can perhaps gain some insight by comparing the asymptotic estimate for return times to the scaled experimental return times. We see in

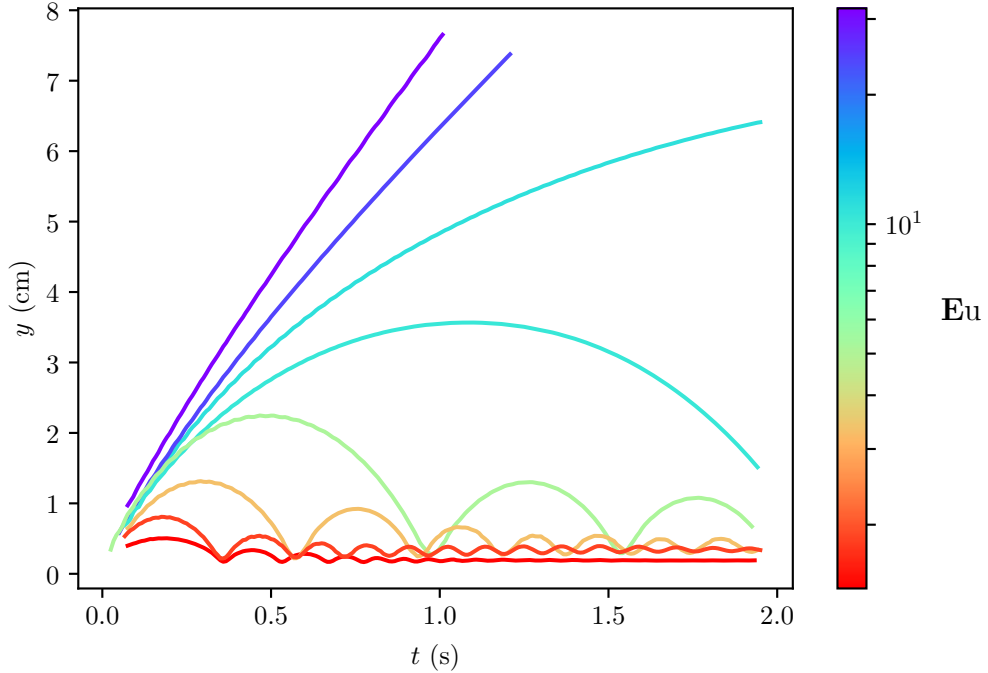


Figure 4.3: Drop trajectories as a function of Eu .

Figure ?? that the long-time scaled non-dimensional time of first bounce in the experiment t_b/t_c , compares poorly to the asymptotic estimate for returns t_f in the limit of small Eu_+ , this is due to the use on long-time scaling for drops with $y/L \ll 1$.

The covariance of Im with Eu is shown in Figure 4.7. Predictably, there is quite strong correlation between the dimensionless groups. We also see that $\text{Im} < 1$ for all drops. Using an OLS regression, we find the model $\text{Im} \sim (0.012 \pm 0.003)\text{Eu} + (0.212 \pm 0.036)$ with $R^2 = 0.59$.

We should note that there are several kinds of systematic error that influence our data. We assume that drop translate purely along the central axis of the electric field, but in practice, despite the improvement in surface charge density uniformity produced by corona charging, there are still local areas of especially high charge density. In principle, this kind of error should become small for drops which are far enough away from the charge distribution, that the geometry of the charge distribution disappears, and the electric field looks like that due to a point charge. Another form of error is in the initial velocity as it appears in Eu . Because we usually lose the first few frames of video due to camera shake transients at the start of the low-gravity experiment, we will consistently underestimate U_0 because the

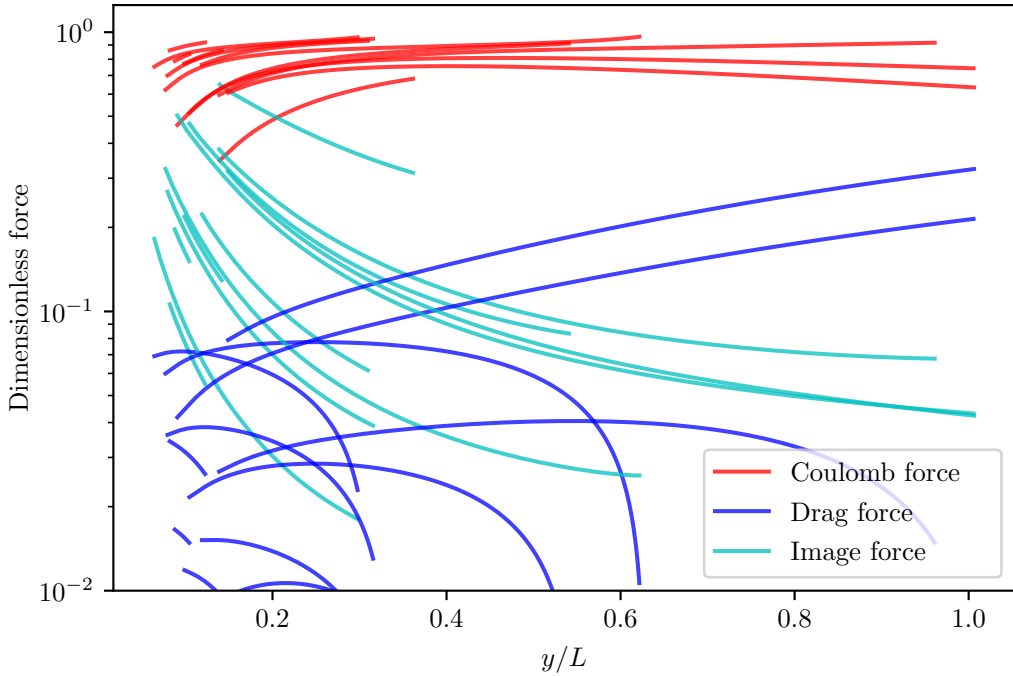


Figure 4.4: Simulated forces acting on the drop. Experiments are shown by order of increasing apoapse.

drop will already have decelerated significantly during that period of time. The primary sources of random error are the effect of contact line hysteresis on the drop initial velocity, and of the variance in the MLE parameter estimates.

4.3 Impact Dynamics

Check the Oh numbers. Very little work to date on drop impacts outside of two regimes: first, very low Re viscous drop spreading driven by capillary forces at the contact line, and second, impacts at “high” We . There has been some computational work with impacts at $\text{Re} = 1.4$ (Fukai *et al.*), but the results are suspect as the model neglects uncompensated Young’s force at the contact line (which is the dominant spreading force for low Re impacts). Of course models for dynamic contact lines in general remain controversial, even for ordinary spreading of liquids, despite decades of work in the area.

Naively neglecting dimensionless groups governing the dynamic contact line, the pertinent dimensionless groups for isothermal droplet impacts are

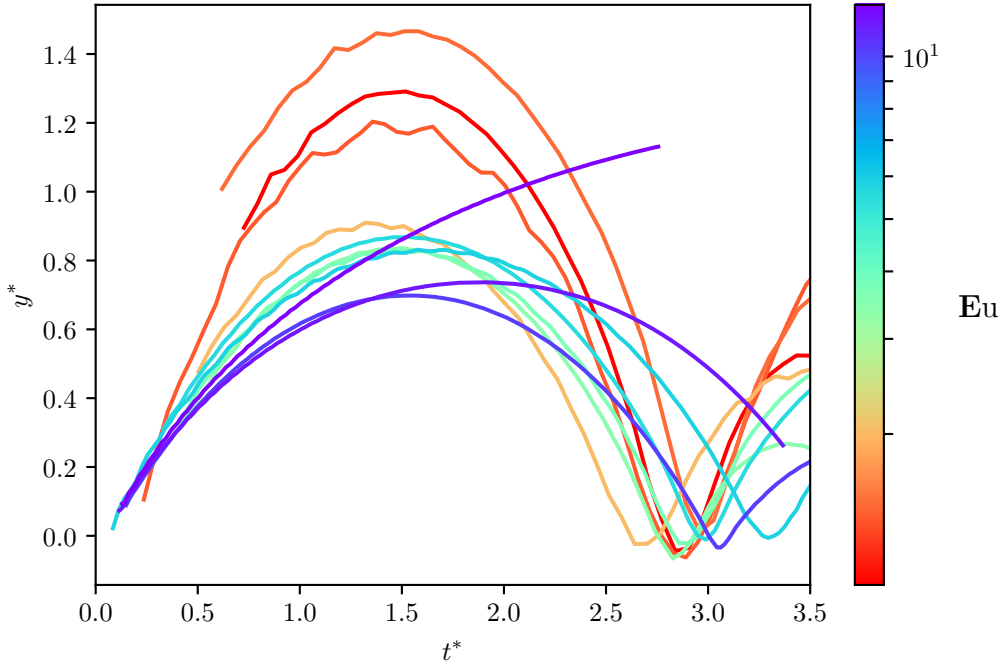


Figure 4.5: Non-dimensional trajectories with the short-time scaling.

the Weber number $\text{We} = \frac{\rho U^2 R_d}{\sigma}$, which is a ratio of droplet inertia to surface tension, the Ohnesorge number, $\text{Oh} = \frac{\mu}{\sqrt{\rho \sigma R_d}}$, which is a ratio of viscous to inertial and surface tension forces, and the Bond number, Bo , defined previously. The dynamics of spreading are characterized primarily by We and Oh . Additionally the final stages of spreading depend strongly on θ_e , which is the static contact angle. The Weber number scales the *driving force* of the impact. In the more familiar case of high We the drop liquid bulk is driven radially outward by the impact induced pressure gradient, whereas in the case of small We the liquid is pulled outwards by capillary force (e.g. uncompensated Young's force) at the contact line. The Ohnesorge number, by contrast, scales the force that *resists* spreading. For large Oh the resistive force is viscous, whereas for low Oh the force is inertia.

We observe average drop impact $\text{Oh} \approx 2.18 \pm 0.36$, and $\text{We} \approx 0.28 \pm 0.22$. Thus impact velocity plays little role in the spreading dynamics of the bounces, and viscous effects are important but do not dominate inertia. Notably we observe underdamped oscillations of drop interfaces during impact. according to (Schiaffino, 1997) viscous forces play a role in the final (which? describe) stage of spreading even for drop impact at very low Oh . In the regime of intermediate viscosity, following spreading the oscillations of

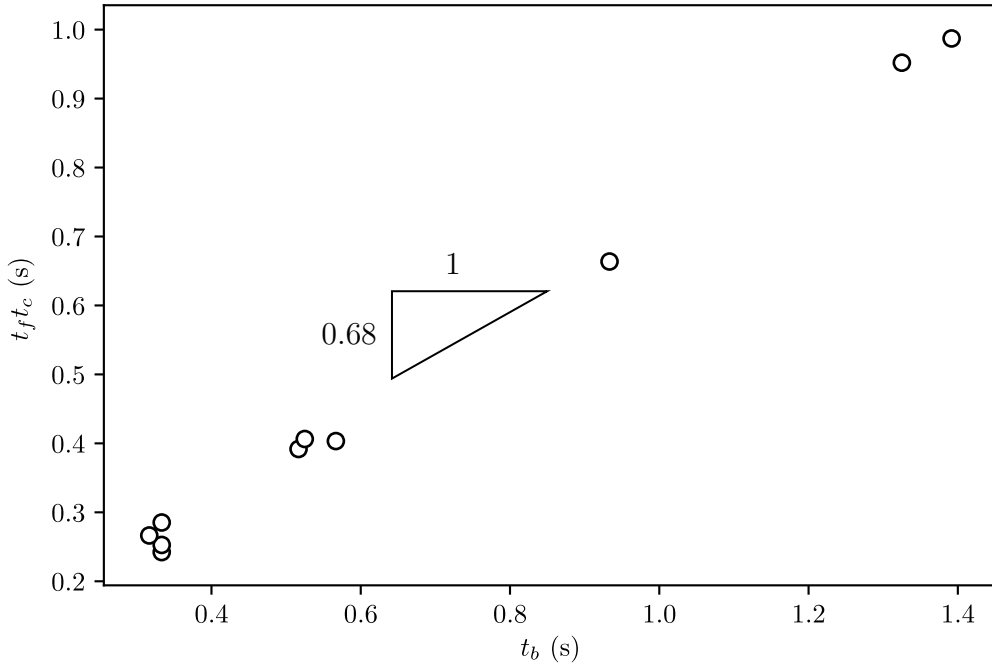


Figure 4.6: Dimensional time of flight asymptotic estimates t_f compared with experimental bounce times.

the interface are damped with a characteristic time that is generally longer than the spreading time (again, given by $t_c \sim (\sigma/\rho R_d^3)^{1/2}$). The celebrated Hoffman-Tanner-Voinov law, which relates the contact line velocity U_c of an isothermal spreading process to the static contact angle θ_e to the dynamic advancing contact angle θ_a by

$$\frac{\mu U_c}{\sigma} \approx \kappa (\theta_a^3 - \theta_e^3),$$

where $\kappa \approx 0.013$ is an empirical coefficient extracted from Hoffman's data. The Hoffman-Tanner-Voinov law implies that the transition between low We inviscid and viscous regimes occurs at $\text{Oh} \sim \mathcal{O}(10^{-2})$ rather than $\text{Oh} \sim \mathcal{O}(1)$ given by a naive scaling.

In $1-g_0$, for Weber numbers > 0.4 , impact recoil behavior on a superhydrophobic surface is normally dominated by damping from contact line hysteresis. However, for the low Bond and Ohnesorge numbers occurring in free-fall, the droplet impact dynamics additionally include electrohydrodynamic surface wettability effects. This is qualitatively discussed in terms of trends in coefficients of restitution and dimensionless contact time.

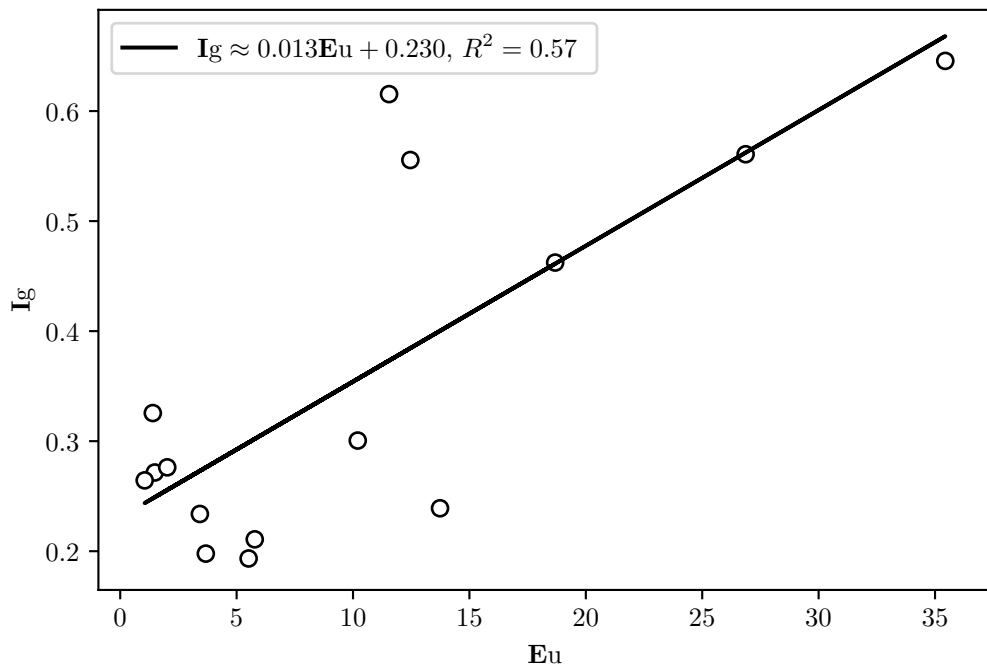


Figure 4.7: Experimental covariance between Eu and Ig.

Some notes:

- Schiaffino, 1997

4.4 Conclusions

-conclusions. -future directions.

Appendices

Appendix A

Parallel Plate Method

Since, by the earlier scaling, we presuppose the source of the drop bouncing behavior to be primarily Coulombic in origin (as opposed to dielectrophoretic), the drop must have some free charge in addition to the charge induced by the electric field. Whether this free charge arises due to contact charge or field-induction To measure this charge concurrent methodologies were used. We determined the drop free charge by observation of the deflection of the drops in the region of a known uniform field in a fashion inspired by Millikan's famous experiment to determine the fundamental charge of the electron.

Drops were jumped in free-fall from a superhydrophobic surface placed between the plates of a parallel plate capacitor of known uniform electric field. The surface was charge neutralized. Since the drop initial velocity U_0 is parallel to the electric field, the drops are inertial in the direction of the electric force, and neglecting the effect of image charges mirrored across the conductors, we can determine the magnitude of the drop charge by a balance of Coulombic force and inertia given by the equation of motion

$$y'(t) = q\mathbf{E}.$$

Since the drag is negligible in the inertial limit we can find the charge q by fitting a second-order least squares polynomial to the measured drop positions, equating the t^2 term to the constant acceleration, and dividing by the known, constant magnitude of the electric field.

A 200-880 VAC source with a full wave bridge rectifier circuit was prototyped on perf-board for initial experiments to measure drop charge. The circuit was analyzed on an laboratory oscilloscope to verify that the AC component of the signal was appropriately small (13 mV at 35 kHz). Current was determined to be a relatively low 80 μ A. The high-voltage source terminals were led to two parallel polished 150x150 mm aluminum plate electrodes.

The electrodes were mounted on an insulated 80/20 extruded aluminum rail for ease of adjustment. All drop charge experiments were conducted with an electrode spacing of 28.30 mm. With this spacing the calibrated electric field between the plates was $E \approx 35\text{kV/m}$. The electrodes were electrically isolated from the drop rig by two alternating layers of 4 mm thick PMMA sheet and Kapton tape. Potential across the plates was measured periodically with a load-impedance corrected multimeter to account for battery depletion. The typical capacitor rise time of the plates was measured to be 1.4 s, thus to make the most economical use of the brief window a low-gravity a weighted switch was set by hand prior to the drop to close the high-voltage circuit, but which passively safed the system at the resumption of $1-g_0$ conditions in the tower. From a survey of literature we suppose the drop charge, if they are indeed charged by contact with PTFE, to be some function of the drop volume and the residence time on the superhydrophobic surface. However, sweeping though drop volumes over a series of drop tower experiments we find little correlation between drop volume and free drop charge.

A brief screening experiment was conducted which alternated the polarity of the field by switching the positive and negative terminal leads between plates. Qualitative observations of drop electrode preference seem to indicate that the assumption of small polarization stress was well founded. Following this a orthogonal array 3^2 factorial design experiment with two replicates was conducted to test the effect of varying drop volume and surface stay time on free charge at the time of jumping. It was hypothesized in accordance with previous studies [ref], that free charge would increase for levels of both factors. ANOVA analysis in R of the linear multiple regression model for the data set indicates that neither drop volume ($p = 0.105$), nor surface stay time ($p = 0.358$) is significant at the 95% confidence level. The overall model F-statistics (2.177 in 2 and 13 degrees of freedom), and coefficients of determination ($r^2 = 0.2509$) indicate that the linear model neither fits the data particularly well, nor does it offer an improvement over the mean model. The mean charge was determined to be positive $2.3 \cdot 10^{-11} \text{ C}$, with a standard deviation of $1.8 \cdot 10^{-11} \text{ C}$.